

<sup>1</sup>

José D. Ruiz-Álvarez

<sup>2</sup>

Compiled on 15/05/2015 at 01:31



# **1 The CMS experiment at LHC**

The CMS experiment is one of the biggest particle physics experiments on the world. It is located at the ring of the LHC that is the main accelerator managed by CERN, the European Organization for Nuclear Research or Centre Européen pour la Recherche Nucléaire by its french name. This center constitutes the biggest center for research on particle physics all over the world. All along its 60 years of existence, from 1954, 21 member states have been joining it, but an overall of 113 countries participate in different ways on this center.

On the present chapter we discuss in detail different aspects of the LHC accelerator and the CMS experiment. In particular we make some emphasis in the CMS sub-detectors related to jets, objects that play the main role on the search that is the main subject of the present work. We also discuss the present state of both machines, their achievements and the challenges that were overcome. Finally, also the expectations and goals for the upcoming run II are mentioned.

## **1.1 The Large Hadron Collider**

The Large Hadron Collider, or LHC [1], is a machine that accelerates and collides protons and lead. This machine is the biggest particle collider nowadays with a circumference of 27 km. It also achieves the highest energy by a collider up to present, planned to be 14 TeV at the center of mass of the collision. On the first run of the machine only 8 TeV were achieved, and next run is planned to start with 13 TeV. It's located in French-Swiss border near to Geneva. The tunnel for the machine was carved around 100 m under the ground, 45 m under the Jura mountains and 170 m under the Léman lake with an inclination of around 1.4%, sloping down towards the lake . This machine has used as much as possible old LEP buildings and sites, that was an electron-positron collider built between 1984 and 1989.

The protons and heavy ions accelerated by the machine collide in different points where dedicated experiments are located to detect and study the product from the collisions. The four main experiments located on the LHC ring are CMS [2, 3], ATLAS [4], LHCb [5] and ALICE [6]. The first two are experiments of generic purpose where searches for new physics and also precision measurements are performed. LHCb is dedicated to the physics of the b-quark, and ALICE focuses on

37 the study of the quark-gluon plasma produced from heavy ions collisions. Even if  
38 one of the principal objectives of the construction of the LHC was the search for  
39 the Higgs boson, generic searches on new physics have been conducted from the  
40 very beginning of the first data taking in 2009. Moreover, after the Higgs discov-  
41 ery in 2012 there is a growing effort on the searches for new physics and precision  
42 measurement of the properties of the Higgs.

43 The LHC is a complex machine composed of several parts. The two principal  
44 parts are the injector chain and the main ring. A diagram of the whole CERN  
45 complex can be seen in figure 1.1. The injector chain has different stages that  
46 pre-accelerate protons and heavy ions to be injected into the main ring of LHC.

### 47 **1.1.1 Injector chain**

48 The injector chain begins with the proton source. Protons are extracted via ioniza-  
49 tion of Hydrogen gas in the Duoplasmatron Proton Ion Source. Such extraction is  
50 pulsed, what makes up the first bunch structure. The extracted protons are then  
51 accelerated up to 50 MeV in the linear accelerator, Linac2, that dates from 1978.  
52 After this first stage several steps are followed:

- 53 1. Linac2 injects proton bunches in the Proton Synchrotron Booster (PSB)  
54 where they are accelerated to 1.4 GeV.
- 55 2. From PSB, the protons are delivered to the Proton Synchrotron (PS) where  
56 they reach an energy of 25 GeV. In the PS the bunches are also split from 6  
57 initial bunches to 72 spaced by 25 ns.
- 58 3. Finally, the pre-acceleration chain is finished by the SPS, Super Proton Syn-  
59 chrotron. There the bunches are accelerated up to 450 GeV right before  
60 being inserted into the main LHC ring.

61 The whole pre-acceleration chain has been optimized to obtain the best possible  
62 performance on the final acceleration in the LHC main ring. All parameters are  
63 carefully controlled, for example the number of bunches, the separation between  
64 bunches, the separation between trains of bunches or the injection energy to each  
65 subsystem. It's also remarkable to notice the level of control achieved in the  
66 bunches manipulation, from old subsystems as the PS from 1959 or the newest,  
67 the SPS that dates from 1976.

68 Some recent plans for future accelerator have been studied using the LHC main  
69 ring as injector for a bigger accelerator, for example the so called FCC (Future Cir-  
70 cular Collider) at CERN. The FCC could be built perform proton-proton, electron-  
71 positron or electron-proton collisions, versions that are called respectively FCC-hh,  
72 FCC-ee and FCC-he. The FCC-hh is being designed to achieve 100 TeV of center  
73 of mass energy in a tunnel of 80-100 km of circumference.

# CERN Accelerator Complex

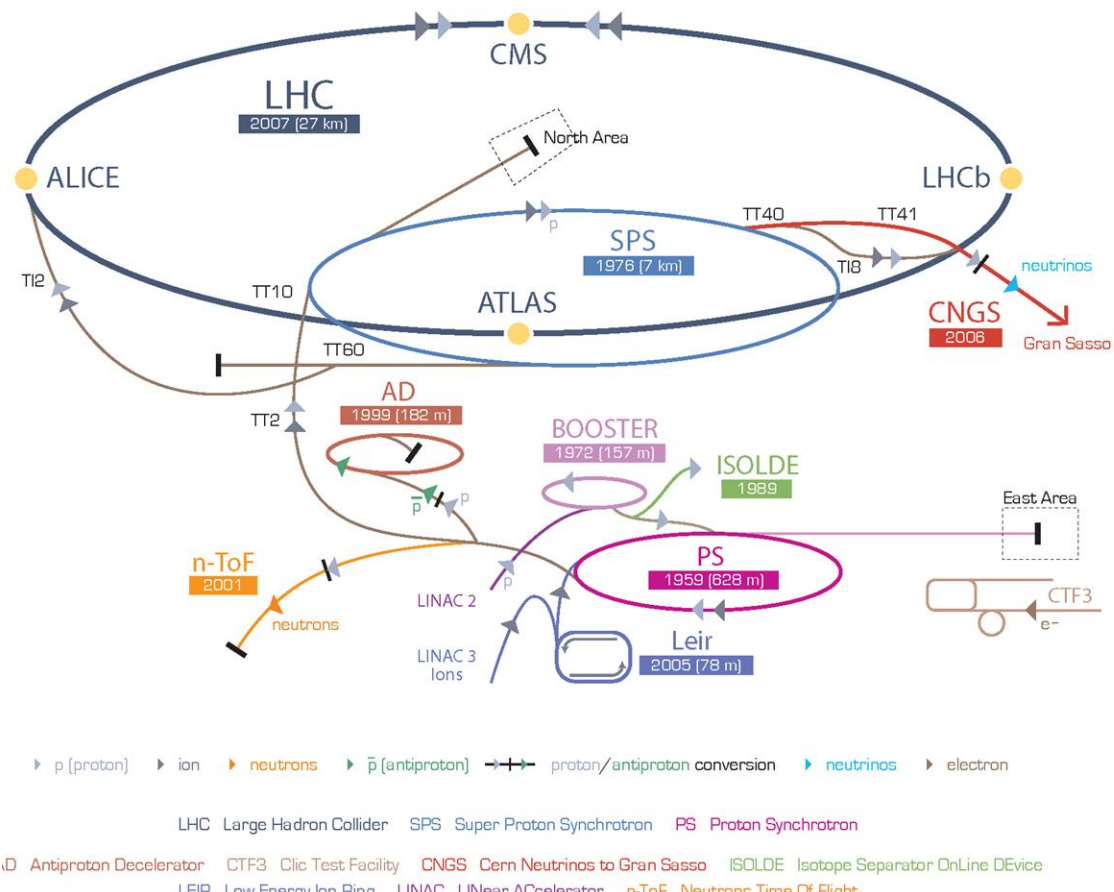


Figure 1.1: Organization of CERN accelerator complex

<sup>74</sup> **1.1.2 Main ring**

<sup>75</sup> The main ring is composed of two rings that accelerate the proton bunches in  
<sup>76</sup> opposite directions, clock-wise and counter clock-wise. An schematic view of the  
<sup>77</sup> design of the main ring can be seen in figure 1.2. The rings crosses in different  
<sup>78</sup> points in order to collide the protons and they are divided in eight straight sections  
<sup>79</sup> and eight arcs. In each octant bunches are controlled by dipole magnets. These  
<sup>80</sup> complex magnets, in figure 1.3, need to produce a very strong magnetic field in  
<sup>81</sup> order to be able to bend a 7 TeV beam of protons. This intense magnetic field, 8.33  
<sup>82</sup> T, in opposite directions, is produced by electrical currents that are only achievable  
<sup>83</sup> by means of superconductivity. All the 1232 dipoles operate at a temperature of  
<sup>84</sup> 1.9 K, under cooling by liquid helium. They also operate under ultra-high-vacuum.  
<sup>85</sup> The beam lines with a pressure less than  $10^{-9}$  mbar and the whole dipole system  
<sup>86</sup> with  $10^{-6}$  mbar, that serves also as insulating system from the surroundings. In  
<sup>87</sup> addition, the LHC main ring has other magnets that focus and correct different  
<sup>88</sup> characteristics of the beam: 520 quadrupoles, 2464 sextupoles, 1232 octupoles.

<sup>89</sup> **Luminosity**

<sup>90</sup> In collider physics, such as the LHC, the figure of merit is the luminosity, given in  
<sup>91</sup> equation 1.1. The number of events per second is proportional to the luminosity,  
<sup>92</sup> hence is the quantity to be maximized by the design and operation of the acceler-  
<sup>93</sup> ator. The collider characteristics depend on the number of bunches in the ring  $n_b$ ,  
<sup>94</sup> the number of protons per bunch  $N_b$ , the revolution frequency  $f_{rev}$ , the relativistic  
<sup>95</sup> gamma factor  $\gamma$ , the normalized rms transverse beam emittance  $\epsilon_n$  and the beta  
<sup>96</sup> function at the interaction point  $\beta^*$ . The denominator on 1.1 can also be rewritten  
<sup>97</sup> in terms of the horizontal and vertical width of the bunches at the crossing,  $\sigma_x^*$   
<sup>98</sup> and  $\sigma_y^*$ . In addition, there is the geometric reduction factor ( $R$ ) that introduces  
<sup>99</sup> a dependence on the crossing angle of the bunches at the interaction points. In  
<sup>100</sup> table 1.1.2 can be found the LHC beam parameters at injection and collision.

$$L = \frac{n_b N_b^2 f_{rev} \gamma}{4\pi \epsilon_n \beta^*} R = \frac{n_b N_b^2 f_{rev}}{4\pi \sigma_x^* \sigma_y^*} R \quad (1.1)$$

<sup>101</sup> At the crossing points, the number of events coming from collisions and produced  
<sup>102</sup> via a specific process, is directly proportional to the luminosity provided by the  
<sup>103</sup> collider, as in equation 1.1.

$$N_{events} = L \sigma_{process} \quad (1.2)$$

<sup>104</sup> where  $\sigma_{process}$  is the cross section of the process.

<sup>105</sup> The total cross section of a proton-proton collision from the crossing of two  
<sup>106</sup> bunches at 14 TeV is 100-110 mb [7], from three different scattering processes:

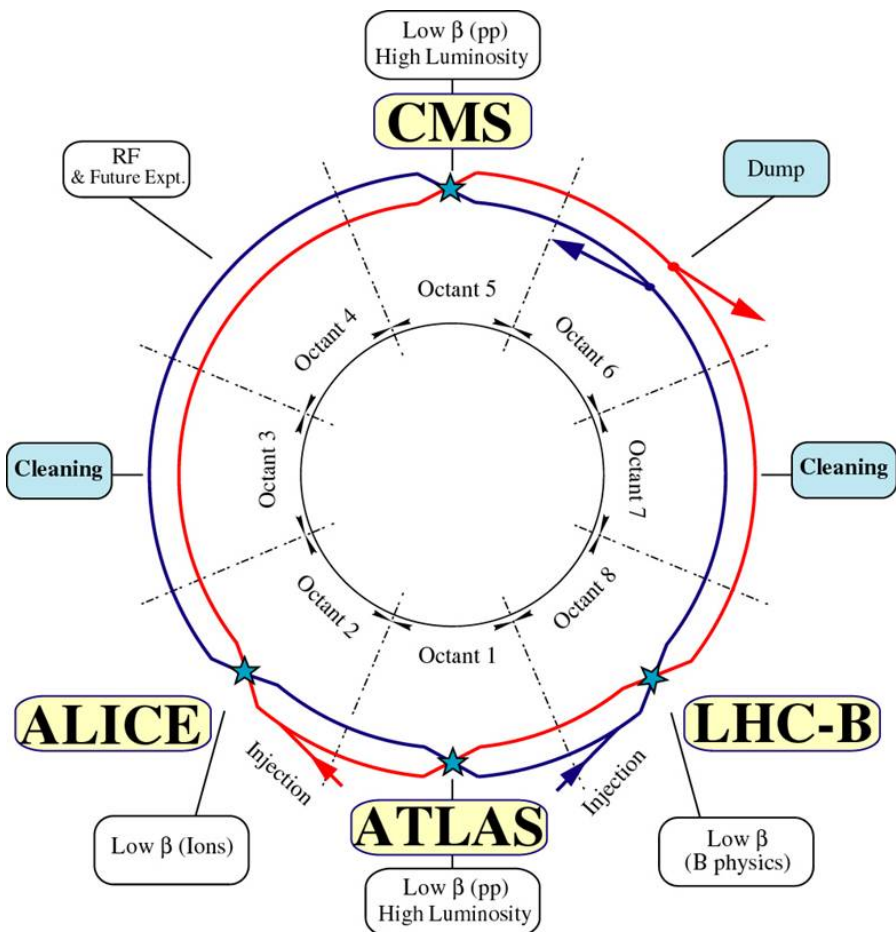


Figure 1.2: Schematic of the LHC main ring design.

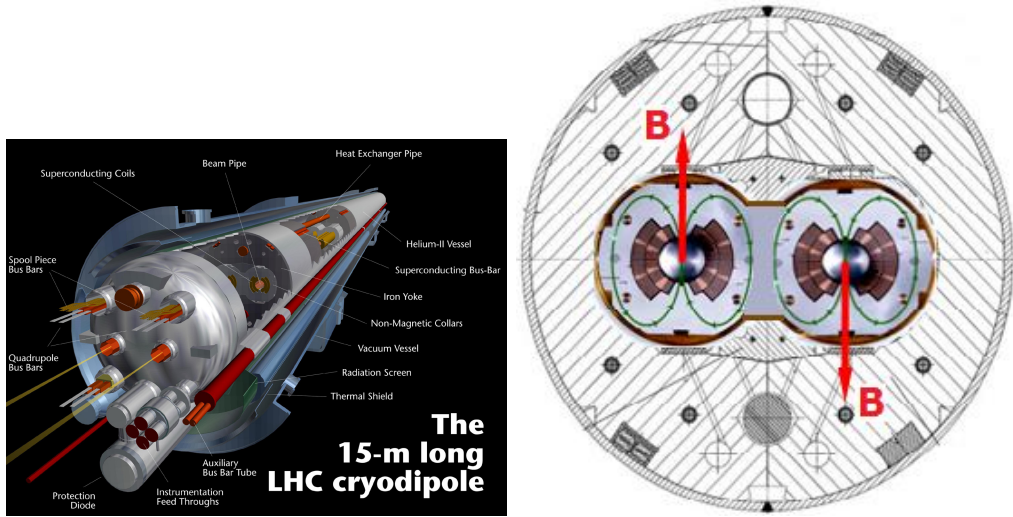


Figure 1.3: Design of LHC cryodipole and the magnetic field that bends the beam in the main ring.

elastic, diffractive and inelastic. In the elastic scattering the protons only exchange momenta but their structure remain unchanged, that is the case for the majority of collisions. In diffractive scattering momenta is exchanged and also new particles are produced in addition to the two final protons. Finally, in inelastic scattering, the constituents of the protons, the partons, interchange a big amount of momentum and produce a large quantity of particles. The inelastic processes contribute less than diffraction to the total cross section. While inelastic collisions produce particles in the central rapidity (defined in 1.2.1) region, diffractive and elastic final products have a large rapidity. Only in the hard interactions, inelastic scattering, color is exchanged, being the reason to fill up the central rapidity

Parameter/units	Injection	Collision
Energy [GeV]	450	7000
Luminosity [ $\text{cm}^{-2}\text{s}^{-1}$ ]		$10^{34}$
$k_b$ Number of bunches		2808
Bunch spacing [ns]		24.95
$N_b$ intensity per bunch [protons/bunch]		$1.15 \times 10^{11}$
Beam current [A]		0.58
$\epsilon_n$ normalized rms transverse beam emittance [ $\mu\text{m}$ ]	3.5	3.75
$f_{rev}$ revolution frequency [kHz]		11.25

117 region.

118 From the crossing of two bunches not only one proton-proton interaction is  
119 expected. In average, 25 interactions are expected for each crossing. From them,  
120 only one is coming from an inelastic collision, that is the type of process of more  
121 interest for detectors as CMS or ATLAS. This fact puts an additional difficulty  
122 to the detectors in order to extract the hard interaction from all the elastic and  
123 diffractive collisions happening at same time. Such phenomena is known as Pile-  
124 Up, an illustration of a collision with high pile-up can be found on figure 1.4 as  
125 seen by the CMS detector.

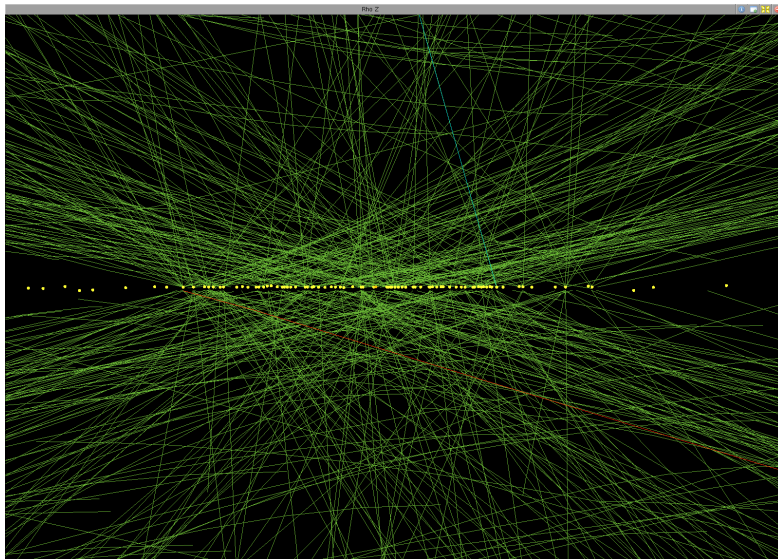


Figure 1.4: High pile-up event (78 interactions) seen by CMS detector. Event 35655522, from 198609 run, lumi 56, recorded on 2012. Image credit: Andre Holzner ©CERN

### 126 1.1.3 Run 1

127 On February 10 of 2013 the first stable run of the LHC reached an end. This run,  
128 now called Run 1, started on November 20 of 2009. LHC was originally planned  
129 to start in 2008, but an incident on one of the electric connections of one of the  
130 magnets forced to stop on the 19th of September of the same year. From the  
131 restart in 2009, the energy was augmented from 450 GeV to 4 TeV per beam. The  
132 23th of September 2009 the first collisions were detected by the experiments. One  
133 week after, the achieved center of mass energy was  $\sqrt{s} = 2.36$  TeV, already higher  
134 than Tevatron (0.98 TeV).

135 In 2010, from 30th March to 6th December 3.5 TeV per beam were reached de-  
 136 livering near  $50 \text{ pb}^{-1}$ . With the same energy, approximately  $6 \text{ fb}^{-1}$  were delivered  
 137 in 2011.

138 In 2012, the center of mass energy reached one additional TeV,  $\sqrt{s} = 8 \text{ TeV}$ ,  
 139 and around  $20 \text{ fb}^{-1}$  of integrated luminosity were delivered between April and  
 140 December. On figure 1.5 can be seen the progress of the recorded luminosity by  
 141 CMS for 2010-2012 period. The first six weeks of 2013 were devoted to proton-lead  
 142 collisions.

143 After this very successful run, the LHC has been stopped for more than a year  
 144 for repair and maintenance of different systems in the experiments and in the LHC  
 145 itself to achieve higher energies. After this period, known as Long Shutdown or  
 146 LS1, the LHC is planned to restart a new run on the early spring of 2015.

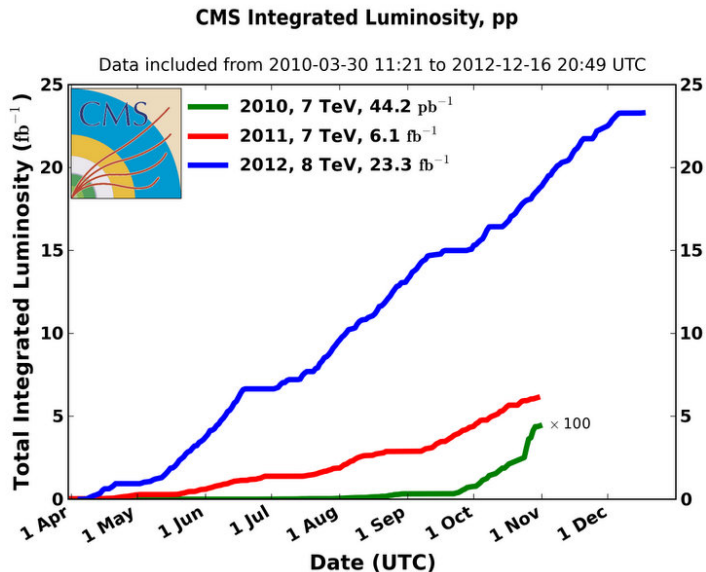


Figure 1.5: CMS integrated luminosity for proton-proton collisions delivered by LHC. ©CERN

#### 147 1.1.4 Other experiments at LHC

148 On the main ring there are several experiments depending on the collisions de-  
 149 livered by the LHC main ring. The biggest are CMS [2] and ATLAS [4], both  
 150 of them generalist experiments designed to do precision measurements as well as  
 151 new physics searches. Mainly recording proton-proton collisions, they have also

152 recorded lead-lead and proton-lead collisions during the run 1. Both of them were  
153 designed for high instantaneous luminosity,  $L = 10^{34} \text{cm}^2\text{s}^{-1}$ .

154 In addition, there are two other experiments designed for specific purposes. The  
155 LHCb [5] that focus on the study of the physics of the b-hadrons, specially related  
156 to the CP violation, and ALICE [6] built for the study of strongly interacting matter.  
157 The first of them record proton-proton collisions at an instantaneous luminosity  
158 of  $10^{32} \text{cm}^2\text{s}^{-1}$  and the second record ion-ion collision with  $L = 10^{27} \text{cm}^2\text{s}^{-1}$ .

159 The CMS experiment is going to be described in detail in section 1.2. In the  
160 following sections we are going to present very briefly the other three experiments  
161 mentioned above.

## 162 ATLAS

163 The ATLAS experiment (A Toroidal LHC ApparatuS) is the biggest LHC experiment.  
164 It's located at point one, as displayed on figure 1.2, on the LHC main ring.  
165 It's a cylindrical detector similar to CMS, about 45 meter long, 25 meter high, and  
166 weights around 7000 tons. ATLAS main components are, from inside to outside, a  
167 tracking system, an electromagnetic calorimeter, a hadron calorimeter and muon  
168 chambers. In between these subsystems there is an internal solenoidal magnet and  
169 a set of external toroidal magnets. The detector design is presented on figure 1.6.

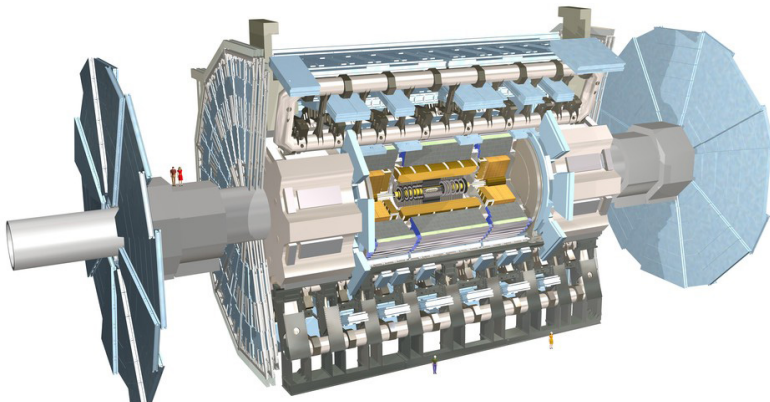


Figure 1.6: ATLAS detector internal view. ©CERN

170 On the human resources side, ATLAS experiment configures a collaboration  
171 of around 3000 persons, coming from 117 universities around the world, from 38  
172 countries. Thirty percent of the collaboration are students.

173 **LHCb**

174 LHCb detector, hosted at point 8 of the LHC main ring, has a different design than  
175 CMS and ATLAS. Smaller than these, its design mainly focus to be able to detect  
176 particles produced close to the beam direction. This is the reason why it is not  
177 cylindrically but conically shaped, in two detection arms 1.7. It also has the same  
178 main parts, a tracking system with a very precise vertex locator, electromagnetic  
179 and hadron calorimeters, muon chambers and magnets. Its major specificity is  
180 a system that allows to identify different hadrons, the RICH detectors, a crucial  
181 feature for the study of strong interacting matter. It measures 21 m long, 10 m  
182 high and 13 m wide, and weights 4500 tons. A view of the detector can be found on  
183 figure 1.7. The LHCb collaboration groups around 700 persons from 50 different  
184 universities over 15 countries.

185 **ALICE**

186 The ALICE experiment (A Large Ion Collider Experiment) is located at point 2  
187 of the LHC main ring, measures 16 m high, 16 m wide and 26 m long, and weights  
188 10000 tons. Designed for heavy ion physics, it is able to detect an extremely high  
189 number of tracks per event. Its main subsystem is the Time Projection Chamber  
190 (TPC), a 90 m<sup>3</sup> gas chamber filled with a mixture of Ne, CO<sub>2</sub> and N<sub>2</sub> operated in  
191 a solenoid of 0.5 T. It allows to measure leptonic and hadronic charged particles in  
192 a momentum range from 0.5 to 10 GeV/c. The experiment structure can be seen  
193 on figure 1.8. ALICE collaboration counts around 1500 people, from 154 physics  
194 institutes in 37 countries.

195 **1.2 The Compact Muon Solenoid (CMS)**  
196 **experiment**

197 The CMS detector, hosted at point 5 of the LHC main ring (see figure 1.2), is the  
198 second biggest LHC experiment. Cylindrically shaped, measures 15 m of diameter  
199 and 28.7 m long, and weights 14000, making it the heaviest LHC experiment. Its  
200 subsystems are concentrically located from the collision point in the beam line. Its  
201 main characteristic is the strong 3.8 T solenoid magnet. A representation of the  
202 detector can be found in figure 1.9. The CMS collaboration is formed by around  
203 2600 scientists, of which 900 are students, from 181 institutes over 41 countries.

204 CMS has been designed to be able to do very precise identification of parti-  
205 cles originated from the collisions and their properties. For the measurement of  
206 the momentum of the charged particles, CMS counts with a very strong magnet  
207 that allows to bend very energetic particles. In addition, the calorimeters allow to

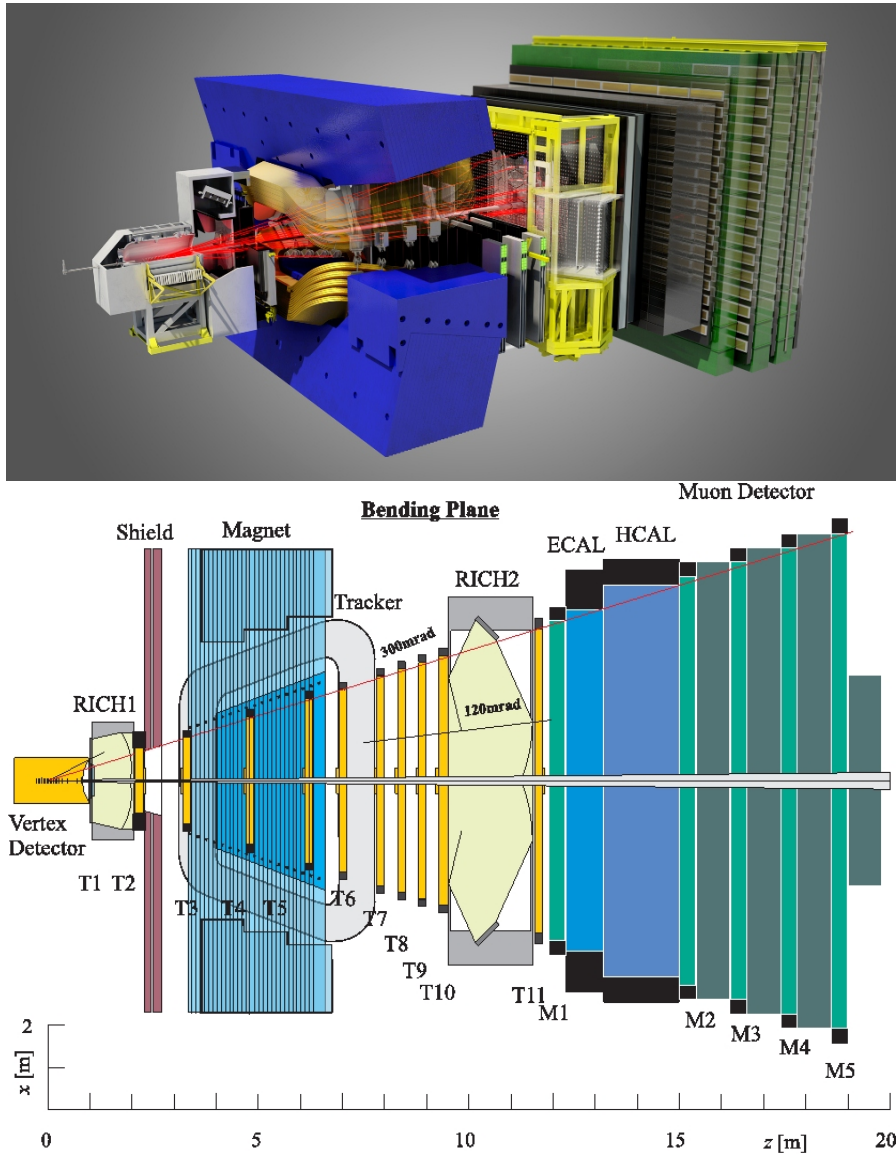


Figure 1.7: LHCb detector internal view [top] and view from the top [bottom].  
©CERN

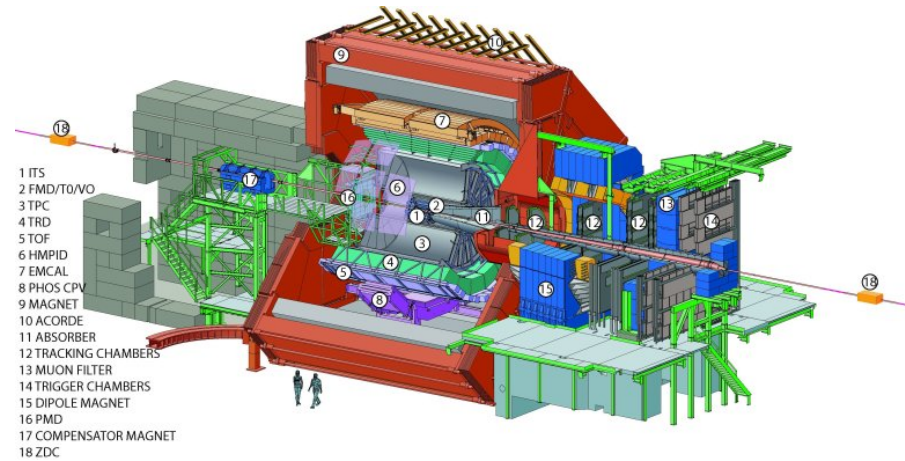


Figure 1.8: ALICE detector internal view. ©CERN

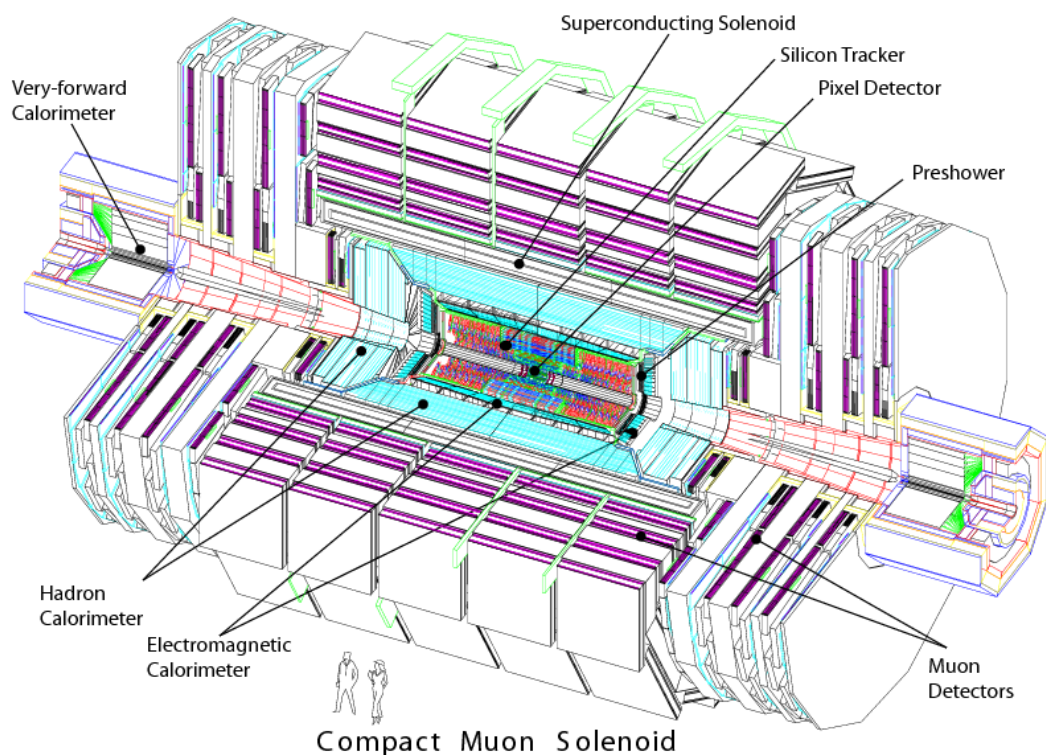


Figure 1.9: CMS detector internal view. ©CERN

measure accurately the energy from hadrons, electrons and photons. At the most external layer, the muons chambers measuring muons properties, and in the innermost the tracking system that reconstructs the collision points and the charged particles tracks. In figure 1.10 can be found a representation of the different subsystems of CMS and how particles are reconstructed from them.

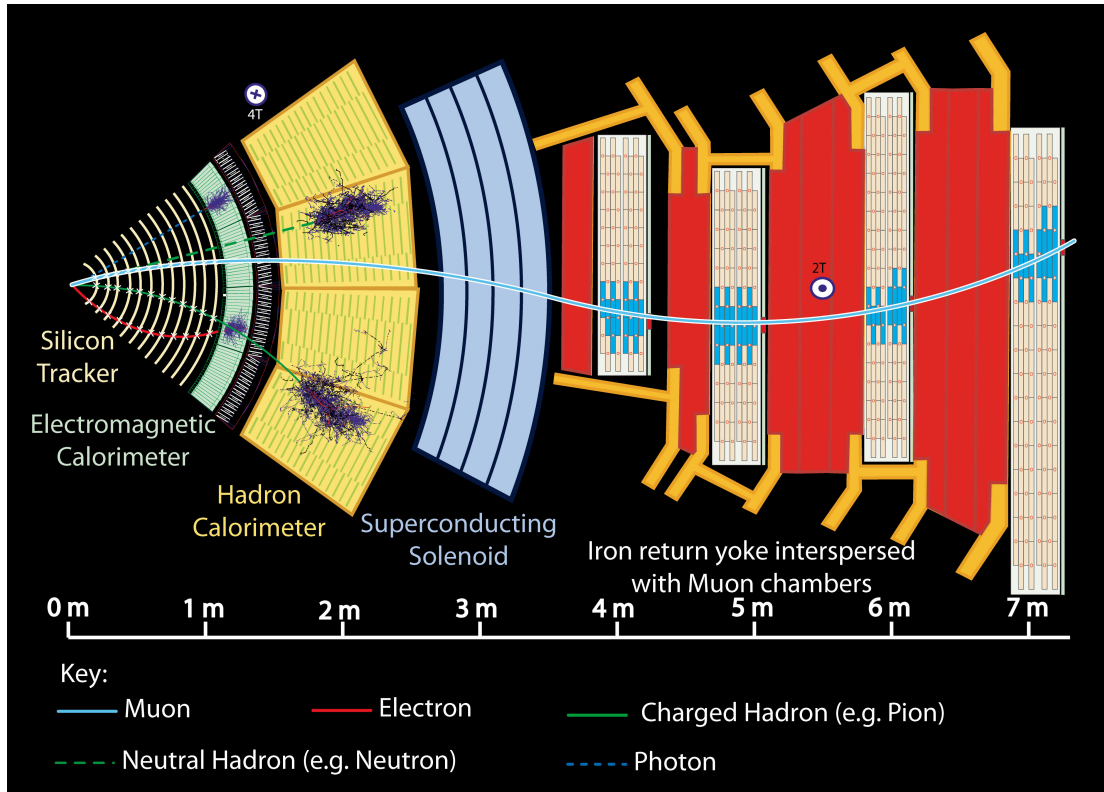


Figure 1.10: CMS sub-detectors and particle identification. ©CERN

### 1.2.1 Coordinate system

The origin of coordinates defined on the CMS detector is located on the nominal collision point, the “interaction point”. From there, the z-axis is defined along the beam pipe line pointing towards the Jura mountains. The positive/negative z-axis directions define the positive/negative sides of the detector. The y-axis is defined towards the zenith and the x-axis towards the center of the LHC ring. Due to the inclination of the LHC plane, this coordinate system is slightly tilted with respect to the true vertical. A representation of the coordinate system definition can be

221 found in figure 1.11.

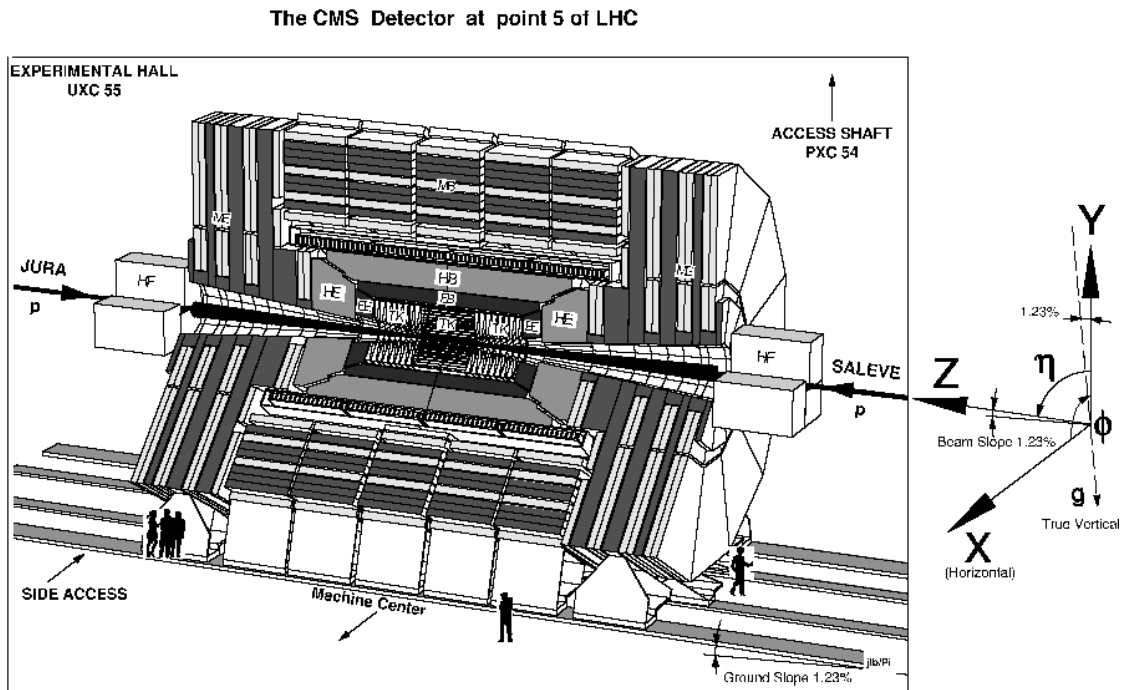


Figure 1.11: CMS coordinate system. ©CERN

222 We can also define two angles: the  $\phi$  angle in the x-y plane from the x-axis  
223 towards the positive y-axis, and the  $\theta$  angle in the z-y plane from z-axis towards  
224 the positive y-axis. In experimental particle physics is preferred to work with  
225 relativistic invariant quantities, reason why instead of working with  $\theta$  we define  
226 the pseudorapidity  $\eta$ , equation 1.3.

$$\eta = -\ln \left( \tan \left( \frac{\theta}{2} \right) \right) \quad (1.3)$$

227 One can define another relativistic invariant quantity, the rapidity  $y$  as from  
228 equation 1.4. With  $\mathbf{p}$  being the momentum vector and  $E$  the energy of a given  
229 particle,  $p_L$  denotes its longitudinal component, that in our case is the same z-  
230 component.

$$y = \frac{1}{2} \ln \left( \frac{E + p_L}{E - p_L} \right) \quad (1.4)$$

231 On the limit that the mass of the particle is very small compared to its momentum,  
232 one can replace approximate the particle energy by the momentum magnitude,

<sup>233</sup> giving rise to the definition of the pseudorapidity in terms of the momentum of  
<sup>234</sup> the particle  $\eta = \frac{1}{2} \ln \left( \frac{\mathbf{p} + \mathbf{p}_L}{\mathbf{p} - \mathbf{p}_L} \right)$

<sup>235</sup> We define also the radial coordinate over the x-y plane, plane that is called  
<sup>236</sup> the transverse plane being orthogonal to the longitudinal direction, the z-axis. In  
<sup>237</sup> such plane are also defined the transverse quantities of particles, as the transverse  
<sup>238</sup> momentum  $p_T$ . Finally, for any two objects an angular distance can be defined in  
<sup>239</sup> the  $\eta - \phi$  plane, as in equation 1.5.

$$\Delta R = \sqrt{(\Delta\eta)^2 + (\Delta\phi)^2} \quad (1.5)$$

## <sup>240</sup> 1.2.2 Magnet

<sup>241</sup> In order to measure the momentum of the charged particles going inside the de-  
<sup>242</sup> tector is crucial to apply the correct magnet field, sufficiently strong to bend very  
<sup>243</sup> energetic particles. The momentum of a charged particle inside an uniform mag-  
<sup>244</sup> netic field can be written as

$$p = \gamma mv = qBr \quad (1.6)$$

<sup>245</sup> where  $B$  is the magnitude of the magnetic field,  $\gamma$  the usual relativistic factor,  $m$   
<sup>246</sup> the mass of the particle,  $v$  its rapidity,  $q$  its charge and  $r$  the bending radius. The  
<sup>247</sup> sagitta of the arc is

$$s = \frac{L^2}{8r} = \frac{qBL^2}{8p} \quad (1.7)$$

<sup>248</sup> with  $L$  the distance the particle moved inside the magnetic filed. Inside a solenoid  
<sup>249</sup>  $L$  is equal to the radius of it.

<sup>250</sup> From relation 1.7 is possible to deduce that the resolution on the momentum  
<sup>251</sup> of the particle has an inverse dependence with the magnetic field and the radius  
<sup>252</sup> of the solenoid, as shown in equation 1.8. From there, for a better resolution is  
<sup>253</sup> needed to increase the magnetic field and the radius of the solenoid.

$$\frac{dp}{p} \propto \frac{p}{BL^2} \quad (1.8)$$

<sup>254</sup> The design of CMS magnet target both features, it utilizes a large solenoid of 6  
<sup>255</sup> m of diameter and 13 m long. It's made of 4 layers of windings of NbTi cable that  
<sup>256</sup> is cooled to 4.45 K in order to achieve the superconducting state. This magnet is  
<sup>257</sup> able to produce an uniform magnetic field inside of it of 3.8 T. Outside the magnet  
<sup>258</sup> 5 wheels and 3 disks of iron are placed in order to return the flux of the magnetic  
<sup>259</sup> field, inducing just a 2 T radial magnetic field outside the solenoid. This iron yoke  
<sup>260</sup> contributes with most of the weight of the detector, 10000 tons. In between the  
<sup>261</sup> iron yoke the muon chambers are placed.

262    **1.2.3 Tracker system**

263    The tracker system has been designed to specifically address the reconstruction  
264    of high  $p_T$  leptons, with particular interest in the isolation of electrons and, as a  
265    consequence, to isolate photons. Also the tracker fulfill granularity requirements  
266    to reconstruct secondary vertexes to tag and reconstruct B-hadrons. The tracker  
267    system is able to reconstruct tracks of particles with at least 2 GeV of  $p_T$  with  
268     $|\eta| < 2.5$ . Charged hadrons are reconstructed with an efficiency of at least 85%  
269    for  $p_T = 1$  GeV and up to 95% for  $p_T$  above 10 GeV. Another important point  
270    that was taken into account is the fact that the tracker is the part of CMS most  
271    exposed to radiation as it is the closest subsystem to the interaction point. The  
272    tracker system was built highly resistant to radiation damage and is expected to  
273    last for around 10 years. The pixel detector only lasts 2 years and was replaces  
274    during LS1.

275    The tracker has been built with three different technologies: Pixels, Silicon  
276    Strips and Micro Strip Gas Chambers (MSGCs). They are arranged concentrically  
277    in cylindrical volumes being the pixel detector the innermost and the MSGCs the  
278    outermost. The CMS tracker extends to a radius of 155 cm and a around 270 cm  
279    on each  $z$  direction. The pixel system is in the region with a radius below  $\approx 20$   
280    cm, the silicon detector between  $\approx 20$  cm and  $\approx 60$  cm, and the MSGCs between  
281     $\approx 70$  cm and  $\approx 120$  cm. The three subsystems are fast enough to work at 25 ns  
282    scale.

283    The pixel system is formed by three barrel layers and two end caps disks covering  
284    radii from 6 cm to 15 cm. It has an approximate active surface of one square meter  
285    with approximately  $40 \times 10^6$  channels with a cell size of 150  $\mu\text{m}$  by 150  $\mu\text{m}$ . This  
286    pixel system allows to obtain three highly precise points that are mainly used for  
287    reconstructing vertexes.

288    The Silicon Strip system is formed by a 5-layer barrel (TIB for Tracker Inner  
289    Barrel) and 10 disks (TID for Tracker Inner Disks) in each end cap. The strips  
290    length is 12.5 cm with a pitch from 61  $\mu\text{m}$  to 122  $\mu\text{m}$  for single-sided strips and for  
291    81  $\mu\text{m}$  to 244  $\mu\text{m}$  for double-sided. It's able to achieve a hit resolution of about  
292    15  $\mu\text{m}$ .

293    The MSGCs systems is composed of 6 layers in the barrel (TOB for Tracker  
294    Outer Barrel) and 11 disks in each end cap (TEC for Tracker EndCap, with a  $\pm$   
295    sign depending on the  $z$  direction). Here the strips are 10 cm length for the inner  
296    layers and 25 cm for outer layers with a pitch from 200  $\mu\text{m}$  to 400  $\mu\text{m}$ , which gives a  
297    hit resolution of 35  $\mu\text{m}$  and 100  $\mu\text{m}$  respectively. The MSGCs and Silicon systems  
298    have an overall active area of around 300  $\text{m}^2$  with  $12 \times 10^6$  channels organized in  
299    more than ten thousand independent modules.

300    In figure 1.12 can be seen the disposition of all the tracker subsystems. From the  
301    design of the tracker system the best resolution on the  $p_T$  measurement is achieved

302 in the  $|\eta| < 1.6$  region, this due to the presence of more layers of detector in the  
 303 different subsystems, as shown in figure 1.13.

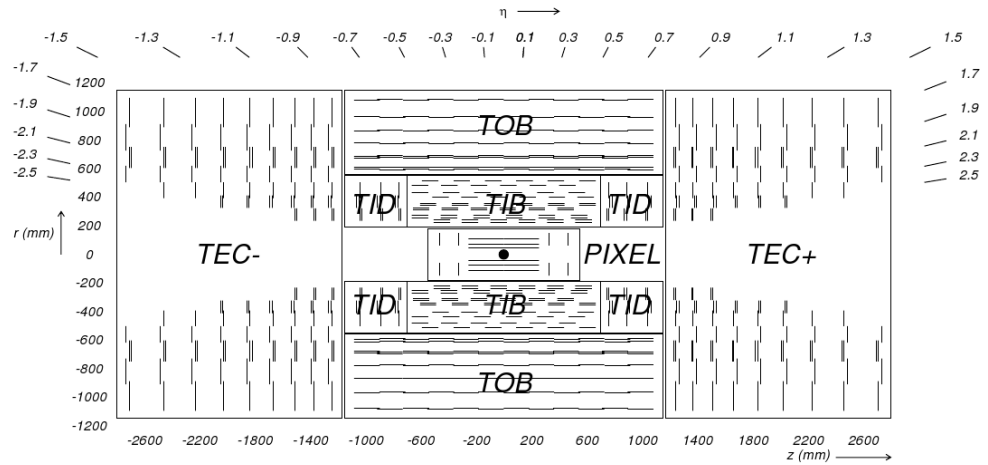


Figure 1.12: CMS tracker system configuration. ©CERN

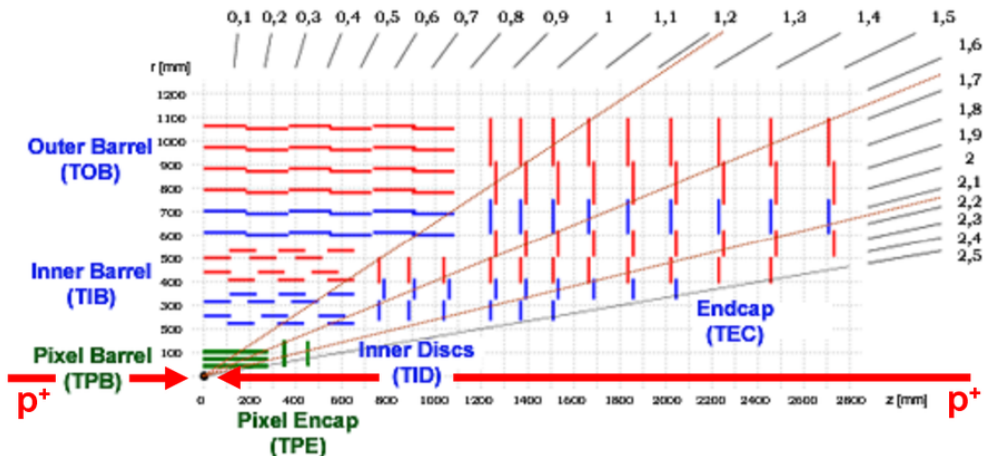


Figure 1.13: Tracker resolution with  $\eta$ . ©CERN

### 304 1.2.4 Electromagnetic calorimeter

305 The CMS ECAL (Electromagnetic CALorimeter) is the detector subsystem de-  
 306 signed to stop photons and electrons to measure their energy. It's an hermetic

307 cylindrical calorimeter made of 61200 crystals in the barrel ( $|\eta| < 1.479$ ) and 7324  
 308 in each end cap ( $1.48 < |\eta| < 3$ ). The crystals material is lead-tungstate that  
 309 is transparent, very dense ( $8.28 \text{ g/cm}^3$ ), has a small Moliere radius (2.2 cm) and  
 310 a short radiation depth ( $X_0 = 0.89 \text{ cm}$ ). This material has been chosen for the  
 311 characteristics already described, but also because it is very fast emitting the scin-  
 312 tillation light (in 25 ns), it has a very good energy resolution and resistance to  
 313 radiation. The crystals are distributed in 36 super-modules, 1700 crystals each, in  
 314 the barrel (EB for ECAL Barrel) and in four 'Dee's, of 3662 crystals each, in the  
 315 end caps (EE for ECAL End cap). In the EB the scintillation light is collected  
 316 by Avalanche Photo-Diodes, or APD, and by Vacuum Photo-Triodes, or VPT, in  
 317 the EE. A preshower system is installed in face of each end cap to allow a better  
 318 discrimination between photons and  $\pi^0$ 's. A representation of the CMS ECAL can  
 319 be found on figure 1.14.

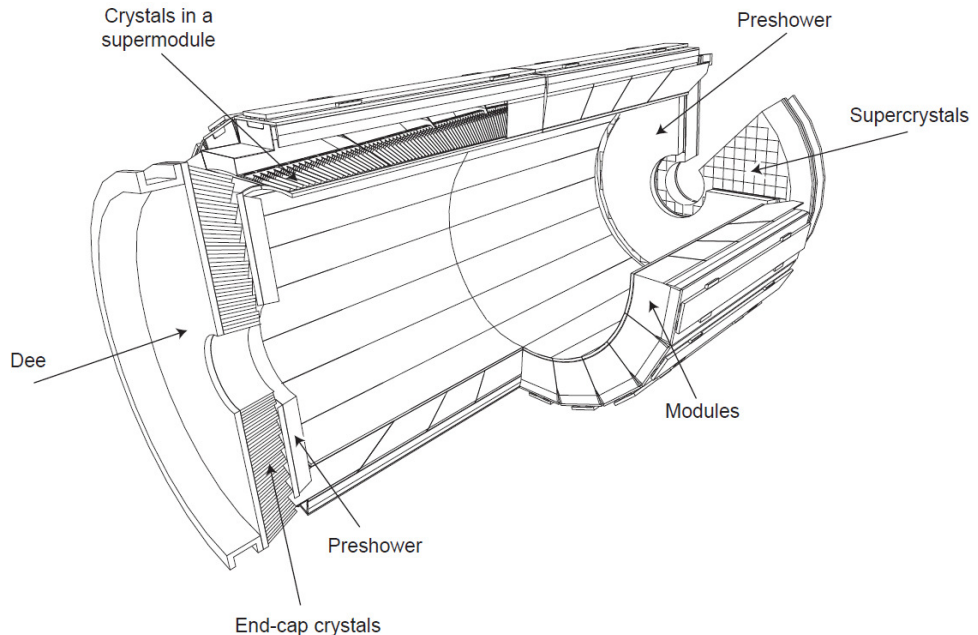


Figure 1.14: CMS ECAL representation. ©CERN

### 320 **1.2.5 Hadronic Calorimeter**

321 The CMS HCAL, for Hadronic CALorimeter, is the subdetector designed to mea-  
 322 sure the energy of hadrons produced in the collisions, mainly the neutral hadrons

323 because the charged hadrons are already traced by the tracker. It's also designed  
324 to measure the missing energy coming from particles not being detected by any  
325 of the subsystems, as neutrinos. It's an hermetic set of subsystems covering up to  
326  $|\eta| < 5.2$ :

- 327 • Hadron Barrel Calorimeter (HB): Covering  $|\eta| < 1.4$  is located between the  
328 ECAL barrel and the magnet.
- 329 • Hadron Endcap Calorimeter (HE): Extends the coverage of the barrel on the  
330 region  $1.4 < |\eta| < 3$ .
- 331 • Hadron Outer Calorimeter (HO): Located outside the magnet, uses it as an  
332 additional absorber.
- 333 • Hadron Forward Calorimeter (HF): Completes the coverage of the system  
334 from  $|\eta| = 3$  up to  $|\eta| = 5.2$ .

335 The CMS HCAL layout is shown in figure 1.15. The system is made of two  
336 parts, an absorber to develop the hadronic showers and a scintillator to measure  
337 the particles energy. The length scale of hadronic calorimetry is designated as the  
338 interaction length corresponding to the mean free path of an hadron in a material.  
339 The HB absorber is made of 40 mm thick steel plate, eight layers of brass plates of  
340 50.5 mm thick, six brass plates of 56.5 mm thick and a steel plate of 75 mm thick.  
341 The HE uses the same absorber but with thicker plates, of 79 mm. Between the  
342 absorber plates a plastic scintillator, Kuraray SCSN81, of 3.7 mm thick is placed.  
343 In the region with  $|\eta| < 1.6$  the achieved granularity is  $\Delta\eta \times \Delta\phi = 0.087 \times 0.087$   
344 and  $\Delta\eta \times \Delta\phi = 0.17 \times 0.17$  in the region with  $|\eta| > 1.6$ . This design gives a total  
345 of 70000 tiles used. The produced light in the HB is collected by optical fibers and  
346 transferred to the Hybrid Photo Diodes (HPDs). This diodes were chosen thanks  
347 to their small sensitivity to the magnetic field, an important feature due to the  
348 proximity of the HCAL to the magnet.

349 The HF design is very different from the rest of the HCAL subsystems. The  
350 most important challenge for the HF is the high resistance to radiation, while in  
351 the central rapidity region 100 GeV are deposited in average in the forward region  
352 is 760 GeV. For this reason it was chosen a Cherenkov detector made of quartz  
353 fibers with a steel absorber. The light produced in the HF is collected by photo  
354 multipliers.

### 355 1.2.6 Muon chambers

356 The muon system of CMS is located at the most exterior layer of the detector due to  
357 the penetration power of this particle. Muons are not stopped by the calorimeters

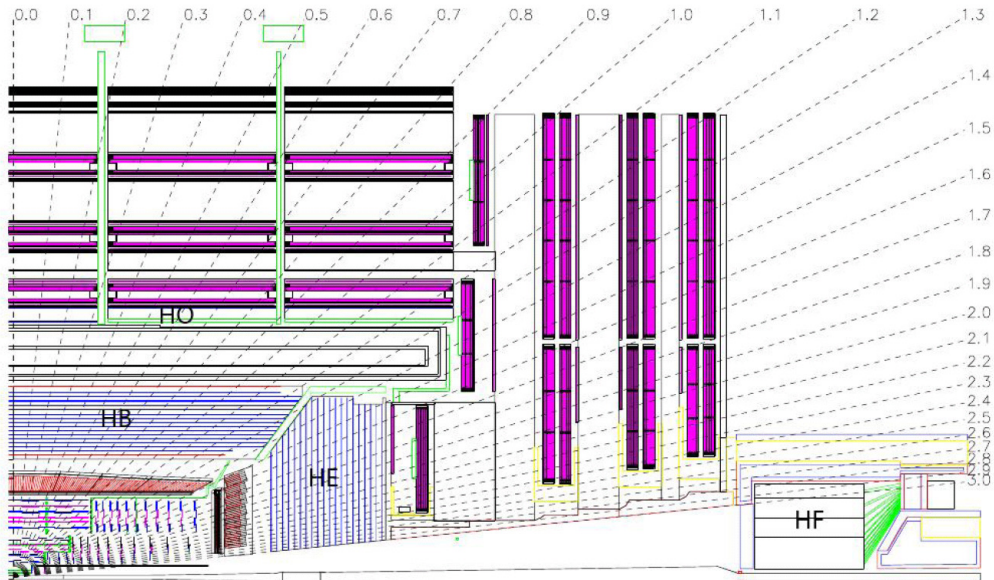


Figure 1.15: CMS HCAL representation. ©CERN

358 and, with neutrinos, they are able to escape the detector. The muon chambers  
 359 are placed in a cylinder around the HO and in disks on the end caps. Three main  
 360 characteristics have been fulfilled from the design: efficient muon identification,  
 361 precision measurement of muon charge and momentum and fast measurement  
 362 to provide trigger capabilities. The moun chambers are made of three different  
 363 subsystems:

- 364     • Drift Tubes Chambers (DT): Located in the region with  $|\eta| < 1.2$  and dis-  
 365         posed in four layers. They consist of individual drift tubes of  $50 \mu\text{m}$  of  
 366         diameter anode wire with two electrode plates creating a drift electric field.  
 367         The wall of the cell act as cathode. The cells are filled with a gas mixture,  
 368         85% Argon and 15%  $\text{CO}_2$ . The tubes are organized in plaques that are also  
 369         organized in SuperLayers (SL) each one made of 4 plaques. The barrel is  
 370         made of 250 DT's disposed in four cylinders separated by iron yokes.
- 371     • Cathode Strip Chambers (CSC): Installed in the end caps, provide a coverage  
 372         up to  $|\eta| = 2.4$  from  $|\eta| = 0.9$ . These chambers are multi-wire proportional  
 373         chambers made of six planes of anode wires with 7 cathode planes. Four  
 374         CSC stations are placed in each end cap. The wires are oriented in azimuthal  
 375         direction while the cathode planes are radially oriented, allowing a complete  
 376         measurement of the position of the particle. This system is able to measure  
 377         with a precision between the  $75 \mu\text{m}$  and  $150 \mu\text{m}$ .

- 378 • Resistive Plate Chambers (RPC): This subsystem is made of gaseous parallel  
 379 plate detectors. This detector is specially useful for triggering as it is very  
 380 fast and have a good position resolution. There are 480 RPC distributed in  
 381 6 layers in the barrel with the DT and in 3 layers in the end caps with the  
 382 CSC, and covers the region with  $|\eta| < 1.6$ .

383 On figure 1.16 can be found a representation of the muon system with the  
 384 different components. The DT and CSC system cover  $|\eta| < 2.4$  without any gap.

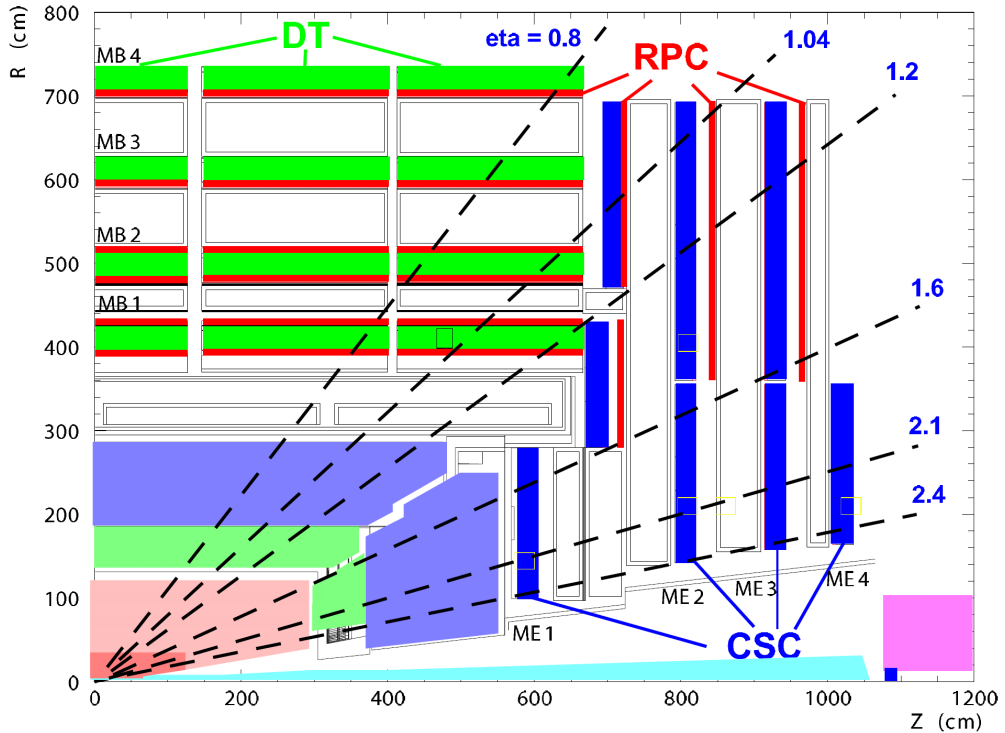


Figure 1.16: CMS muon chambers representation. ©CERN

### 385 1.2.7 Trigger

386 LHC has been designed to provide experiments with proton-proton collisions every  
 387 25 ns, meaning a frequency of 40 MHz. Each recorded event by CMS has a nominal  
 388 size between 0.5 and 1 MB, what means a data flux of around  $10^9 \text{ MB/s} = 1\text{PB/s}$   
 389 that is extremely big for transfer and for storing. Therefore, an on-line selection  
 390 of events has to be done. The trigger system of CMS does this task in two fold,  
 391 a level 1 (L1) and a high level trigger (HLT). The L1 is hardware based and the  
 392 HLT is software based.

393 From the searches conducted at CMS, the interesting events produced on proton-  
394 proton collisions for new physics searches are very rare. The enormous majority of  
395 events coming from proton-proton collisions correspond to well understood phe-  
396 nomena, while new physics events are 'exotic' with regards to the most common  
397 type of events. Then is interesting to keep only a part of the events, what actually  
398 eases the analysis afterward done over the data.

399 The CMS trigger system is designed to keep only 100 kHz tops by the L1 and  
400 300 Hz by the HLT. L1 is reducing the data flux by 2 orders of magnitude and the  
401 HLT another 3 orders of magnitude.

#### 402 **Level 1 trigger**

403 The L1 is designed to trigger over coarse data coming from the calorimeters and  
404 muon chambers, holding data in pipe-lined memories in the front-end electronics.  
405 Therefore, relies on very fast reconstruction of objects coming from this subsys-  
406 tems: muons, electrons, photons, jets and missing energy. This reconstruction  
407 differs from the final reconstruction of the objects, for example a jet for the L1  
408 consists on successive energy deposits in the ECAL and HCAL, while the off-line  
409 reconstruction take into account also the tracker information.

410 The L1 starts from regional data coming from the subsystems which is after-  
411 ward combined in order to build ranked trigger objects in localized regions of the  
412 detector. Global Muon and Calorimeter triggers sort the objects and send the best  
413 ranked to the Global Trigger (GT). Before the GT no events are rejected, is only  
414 with the GT that the selection is applied. The GT combines the information and  
415 can apply topological requirements and take a decision on keeping or disregarding  
416 the event. On figure 1.17 can be found the work-flow of the L1.

417 The L1 cards are distributed between the detector and an adjoin cavern at 90  
418 m distance from the detector. The latency time L1 disposes between the collision  
419 and the taking of the decision is about  $3.2 \mu\text{s}$ . Therefore, the front-end memory  
420 in the cards should be able to keep in memory up to 128 bunch crossings.

#### 421 **High Level Trigger**

422 The HLT take as input the events accepted by the L1 and process them using farms  
423 of commercial processors. The HLT does additional operations on the selected  
424 events making it much slower than L1 processing. In particular, the HLT takes also  
425 into account the tracker information. Consequently, this system is able to take into  
426 consideration the whole information of the detector. However, the reconstruction  
427 of objects done by the HLT differs slightly from the final off-line reconstruction.  
428 The decision taking process takes around 40 ms,  $10^4$  times more than for L1.

429 The events selected by HLT are finally stocked on disks under several paths

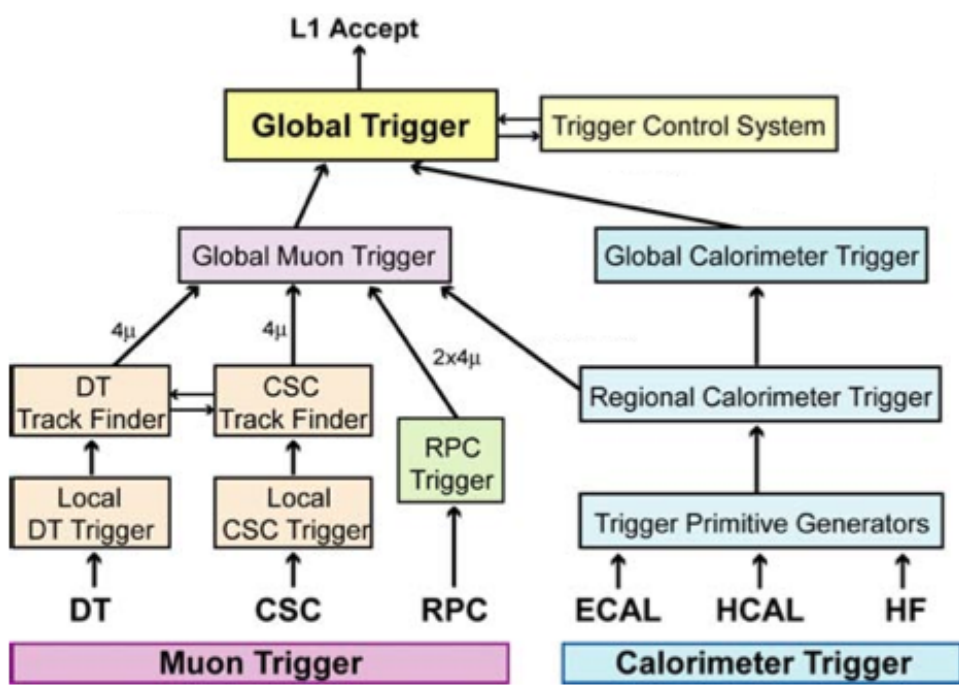


Figure 1.17: L1 architecture. ©CERN

430 depending on the selection performed. There is a constant development of HLT  
431 paths focusing on different analysis requirements in order to obtain the best pos-  
432 sible selection efficiency for specific signal types.

## <sup>433</sup> 2 The Standard Model

<sup>434</sup> Since the Greeks, different theories about the composition and structure of the  
<sup>435</sup> world have been formulated. At ancient Greece these theories were elaborated  
<sup>436</sup> from a philosophical point of view. Nowadays, we count with a very sophisticated  
<sup>437</sup> set of tools and concepts that allowed us to build up a general vision of nature,  
<sup>438</sup> its components and structure. Moreover, on the subject of the constituents, or  
<sup>439</sup> elemental constituents, a theory capable of describing the majority of known phe-  
<sup>440</sup> nomena has been developed. This theory is the Standard Model (SM) of particle  
<sup>441</sup> physics.

<sup>442</sup> This SM relies in two of the more elegant constructs of modern physics and  
<sup>443</sup> mathematics. From the physics side, the quantum field theory; from mathematics,  
<sup>444</sup> group theory. Quantum field theory has born from the understanding of processes  
<sup>445</sup> that take place at very small spatial scales and in a regime where special relativity  
<sup>446</sup> play an important role. To describe such, a major part of the most brilliant minds  
<sup>447</sup> of the 20th century dedicated their life, Paul Dirac, Richard Feynman, Enrico  
<sup>448</sup> Fermi among them. The theory of quantum fields has set in a common place two  
<sup>449</sup> extraordinary achievements of physics: special relativity and quantum mechanics.  
<sup>450</sup> With it we have been capable to describe many phenomena:  $\beta$  and  $\alpha$  decay, solid  
<sup>451</sup> state, among many other.

<sup>452</sup> From the mathematics side, group theory has become one of the most powerful  
<sup>453</sup> tools for particle physicist. However, their development began quite early, with  
<sup>454</sup> Galois around 1830, and was used in other parts of physics, it's with Lie algebras  
<sup>455</sup> and the possibility of describing continuous symmetries that the most important  
<sup>456</sup> step were given. Also, this would have not been possible with the amazing connec-  
<sup>457</sup> tion found by Emmy Noether in 1918. She found that for every conserved quantity  
<sup>458</sup> there is a preserved symmetry. Group theory can be seen, roughly speaking, a way  
<sup>459</sup> to mathematically describe symmetries, group theory became the tool to describe  
<sup>460</sup> systems with conserved quantities.

<sup>461</sup> In this chapter, we present the basics of the SM. We describe its seminal ideas,  
<sup>462</sup> its structure and content and its ultimate consequences. Finally, we close with its  
<sup>463</sup> limitations.

## 464 2.1 Fields, symmetries and interactions

465 From the very beginning of physics, one of the most fundamental questions has  
 466 been how does bodies interact, and what is exactly an interaction. On the first  
 467 type of interaction ever studied by physics, gravity, Newton proposed the con-  
 468 cept of distant interaction, the idea that bodies could interact without being in  
 469 direct contact. But the question on how exactly that distant action was performed  
 470 remained unanswered.

471 During the 19th and 20th century new phenomena were discovered pointing to  
 472 brand new interactions, electricity, magnetism and radioactivity. The very precise  
 473 and complete description of electromagnetism developed by Gauss, Faraday, Am-  
 474 père and finished by Maxwell arrived to describe electricity and magnetism under  
 475 the formalism of only one interaction within the mathematical formalism of classi-  
 476 cal fields. Further works addressed radioactivity, driving to a deeper understanding  
 477 of nature and its composition.

478 For the following discussion, and later, we are going to work in natural units  
 479 for simplicity. In these units the speed of light  $c$  is normalized to unity, as well as  
 480 electron electric charge  $e$ , reduced Planck constant  $\hbar$  and Boltzmann constant  $k_B$ .  
 481 Then, masses and temperature are expressed in energy units, i.e.  $eV$ , and time  
 482 and length in inverse energy units,  $eV^{-1}$ .

483 A classical field is an assignment of a quantity to every point in space and time.  
 484 For physics, the quantity that is attributed is a physical quantity such as mass,  
 485 electrical charge or probability. This quantity can be scalar or vector, giving rise to  
 486 the notion of scalar or vector field, correspondingly. The simplest example, is the  
 487 temperature in a gas, that is a scalar quantity assigned to every point. Another  
 488 example, a fluid can be described in terms of fields, being the velocity of the fluid  
 489 a vector field and its pressure a scalar field. Generic classical electromagnetic  
 490 interactions can be described with the help of one vector field  $\vec{A}(x)$ , the vector  
 491 potential, and one scalar field  $\phi(x)$ , the scalar potential. In the formalism of  
 492 four-vectors from relativistic dynamics one can organize these two quantities in the  
 493 four-potential  $A_\mu = (-\phi, \vec{A})$ . This can be used to define the strength field tensor  
 494  $F_{\mu\nu} = \partial_\mu A_\nu - \partial_\nu A_\mu$ , where  $\partial_\mu = \left(-\frac{\partial}{\partial t}, \nabla\right)$  is the covariant derivative. From the  
 495 tensor is possible to obtain in a very generic and elegant way the equations of  
 496 motion of the free field using the Lagrangian formalism, as in equation 2.1. With  
 497 the Lagrangian density defined in equation 2.2.

$$498 \partial_\mu \left( \frac{\partial \mathcal{L}}{\partial(\partial_\mu A_\nu)} \right) - \frac{\partial \mathcal{L}}{\partial A_\nu} = 0 \quad (2.1)$$

$$499 \mathcal{L} = -\frac{1}{4} F^{\mu\nu} F_{\mu\nu} \quad (2.2)$$

498 It's very important to notice that the equations of motion of the free field are  
 499 invariant under the choice of the four-potential. More precisely, the covariant  
 500 potential is not unique and we can always add the covariant derivative of a scalar  
 501 field,

$$A'_\mu = A_\mu + \partial_\mu \Lambda(x) \leftrightarrow \partial^\mu A_\mu = 0 \quad (2.3)$$

502 and describe the same physics. This non-uniqueness corresponds to the choice  
 503 of a zero-point of the potential very well known in non-Lagrangian formalism of  
 504 electrodynamics. When we choose a specific value for this scalar field,  $\Lambda(x)$ , we  
 505 say that the gauge has been fixed.

506 One can also define a four current vector,  $J_\mu = (\rho, \vec{J})$  with  $\rho$  the electric charge  
 507 density and  $\vec{J}$  the current charge density. Then, plugging in this four current in  
 508 the Lagrangian of the free field, defined in equation 2.2,

$$\mathcal{L} = -\frac{1}{4} F^{\mu\nu} F_{\mu\nu} - A_\mu J^\mu \quad (2.4)$$

509 we can obtain the complete set of equations of motion of the field with charges  
 510 and currents.

511 The transformation stated from equation 2.3 can be understood as a transfor-  
 512 mation of the field. These type of transformations are mathematically understood  
 513 under the group  $U(1)$ , where the generic transformation operator can be written  
 514 as  $U = e^{i\theta(x)}$ . It's said then that the electromagnetic vector potential is *invariant*  
 515 under  $U(1)$  transformations. This property identifies an essential characteristic of  
 516 electromagnetism, its symmetric behavior under  $U(1)$ .

517 From this reasoning the most interesting results are drawn when the same sym-  
 518 metry is imposed to another fields. For example, the kinetic Lagrangian for a  
 519 complex scalar field is  $\mathcal{L} = (\partial^\mu \phi)^* \partial_\mu \phi$ . To perform the transformation on the  
 520 scalar field, it is sufficient to apply the operator as  $\phi' = U\phi$  and  $\phi'^* = \phi^* U^{-1}$ . But  
 521 it's evident that the Lagrangian is not the same after applying such transforma-  
 522 tion. Then, in order to preserve the Lagrangian under  $U(1)$  is necessary to change  
 523 at the same time the derivative. Such transformation is given in equation 2.5,  
 524 where  $g$  is a constant.

$$\mathcal{D}^\mu = \partial^\mu - ig A^\mu \quad (2.5)$$

525 Then, the proposed Lagrangian can be rewritten, including the vector field, as

$$\mathcal{L} = (\mathcal{D}^\mu \phi)^* \mathcal{D}_\mu \phi - \frac{1}{4} F^{\mu\nu} F_{\mu\nu} \quad (2.6)$$

526 that is invariant under  $U(1)$ . An interaction term, of the form  $ig A^\mu \phi^* \partial_\mu$ , between  
 527 the scalar and the vector field, can be derived from the kinematic part of the  
 528 Lagrangian  $\mathcal{D}^\mu \phi)^* \mathcal{D}_\mu \phi$ . This shows that the requirement of the invariance under

529  $U(1)$  of the scalar field lead to the introduction of an interaction with a vector field  
530 controlled by the constant  $g$ . We have also seen that electromagnetic interaction  
531 is described precisely by a vector field and that preserves  $U(1)$  symmetry, which  
532 implies that this symmetry is the connection to electromagnetic interaction, iden-  
533 tifying the interaction itself with the  $U(1)$  symmetry. In addition, using Noether  
534 theorem one can show that  $g$  is a conserved quantity, as the electric charge is.

535 But not only electromagnetism can be described via a continuous symmetry as  
536  $U(1)$ . On 1896 radioactivity was discovered by the french physicist Henri Bec-  
537 querel. Three years after, Marie and Pierre Curie studied in more detail the  
538 phenomenon and found Polonium and Radium elements. And later on, Ernst  
539 Rutherford was able to describe radioactivity as coming in three types, alpha ( $\alpha$ ),  
540 beta ( $\beta$ ) and gamma ( $\gamma$ ). He also noticed that radioactivity was able to change  
541 matter, which allowed him, with also other experiences, to propose an atomic  
542 model, describing elements as basically and external core of negative charges and  
543 a nucleus positively charged. Consequently, This findings implied the existence of  
544 interactions different to electromagnetism, acting at the atomic scale.

545 The interaction that undergoes radioactivity, beta decay, is called the weak  
546 interaction. In 1933 Enrico Fermi made a first theoretical description of this in-  
547 teraction, but only in 1968 Sheldon Glashow, Abdus Salam and Steven Weinberg  
548 were able to describe weak interaction with a symmetry group:  $SU(2)$ . Finally,  
549 the interaction that keeps the nucleus components together, the strong interaction,  
550 was described with  $SU(3)$  group mainly by Murray Gell-Mann in 1963.

551 There have been many attempts to describe gravity with the same formalism,  
552 but up to present such attempts have been unsuccessful. Such question remains  
553 one of the most important problems for modern particle physics.

## 554 2.2 Quantum fields and particles

555 Classical fields, introduced and described in last section 2.1, can be extended to a  
556 quantum theory. Such procedure is known as the quantization of fields and allow  
557 to unify special relativity and quantum mechanics in one theory, Quantum Field  
558 Theory (QFT), to describe the dynamics of systems in such regimes: speed close  
559 to the speed of light on the atomic or smaller scales.

560 Quantum mechanics introduced two fundamental concepts: first, the description  
561 of the system by its states; and second, the identification of an observable with  
562 an operator. The state of a system is identified with a set of quantum numbers  
563 that tell us the characteristics of the system when is at some state. For example,  
564 the hydrogen atom system has energy as quantum number, such that each state  
565 has a value for the energy describing the potential energy contained in the system.  
566 Quantum states are mathematically noted in Dirac notation as a *ket*,

$$|\alpha\rangle = |i, j, k, \dots\rangle \quad (2.7)$$

567 with  $\alpha$  the set of quantum numbers  $i, j, k, \dots$ . This mathematical object lives in  
 568 Hilbert space (a complex space  $\mathbb{C}$  of functions), which conjugate, a *bra*, is noted  
 569  $\langle\alpha|$ , and their internal product  $\langle\beta|\alpha\rangle$ . The numerical value of  $|\langle\beta|\alpha\rangle|^2$  gives the  
 570 transition probability of the system from state  $\beta$  to state  $\alpha$ , and  $|\langle\alpha|\alpha\rangle|^2$  is the  
 571 probability to find the system in state the  $\alpha$ .

572 Physical observables as position, energy or momentum are described by complex  
 573 operators such that to measure their value for a given state, one just have to  
 574 calculate  $|\langle\alpha|\hat{O}|\alpha\rangle|^2$ . The identification of observables and operators is called *first*  
 575 *quantization*. In addition, Schrodinger equation describes the evolution of states,

$$\hat{\mathcal{H}}|\alpha\rangle = i\frac{d}{dt}|\alpha\rangle \quad (2.8)$$

576 with  $\mathcal{H}$  the Hamiltonian of the system. The whole formalism is able to explain  
 577 *quantized* systems, where the quantum numbers are discrete, such as hydrogen  
 578 atom or black body.

579 Several functions or fields can be related to a given state. These functions,  
 580 wave functions, can be used as the states to calculate probabilities. In *second*  
 581 *quantization* wave functions are upgraded into field operators. This procedure  
 582 gives rise to the quantization of the state of the field, which is described by the  
 583 quantum number  $n$  which is definite positive.  $n = 0$  for the fundamental state  
 584 and  $n > 0$  for the excited states. Such excitations of the field are understood  
 585 as physical particles that propagates in space-time, which means that  $n = 0$  is  
 586 vacuum.

587 The first QFT ever created was born from the quantization of the electromagnetic  
 588 field. Quantum Electro Dynamics (QED) is the quantized version of classical  
 589 electrodynamics, that was developed by Tomonaga, Schwinger and Feynman  
 590 around 1960. This theory describes electromagnetic interactions of a charged field  
 591 and the electromagnetic vector field. The charged field excitations correspond to  
 592 electrons and the excitations of the vector fields are photons, responsible of light.  
 593 Electrons are a particle with negative electric charge and orbit around the nucleus  
 594 in atoms. Discovered in 1897 by J. J. Thomson, it was fully described by P. A.  
 595 Dirac in 1928 with the Dirac equation that is the Schrodinger equation for a rel-  
 596 ativistic particle of spin  $1/2$ . Spin, the intrinsic angular momentum carried by  
 597 a particle, can be integer  $(0, 1, 2, \dots)$  or semi-integer  $(\frac{1}{2}, \frac{3}{2}, \dots)$ . The particles with  
 598 semi-integer spin, as electrons, are called *fermions* and particles with integer spin,  
 599 as photons, are called *bosons*. Dirac equation predicted the existence of a particle  
 600 identical to the electron but with positive charge, the positron. It was discovered  
 601 on 1932 by Carl David Anderson.

Up to present days we have found 12 fundamental fermions and 5 fundamental bosons. Fermions are organized in *leptons*, that don't interact strongly, and *quarks*, that do interact strongly. Leptons are as well organized in three families, the electron ( $e^-$ ) and electron neutrino ( $\nu_e$ ), muon ( $\mu^-$ ) and muon neutrino ( $\nu_\mu$ ) and tau ( $\tau$ ) and tau neutrino ( $\nu_\tau$ ). Electron, muon and tau are electrically charged while neutrinos are neutral. Their respective anti-particles are equally organized, positron ( $e^+$ ) with electron anti-neutrino ( $\bar{\nu}_e$ ), anti-muon ( $\mu^+$ ) with muon anti-neutrino ( $\bar{\nu}_\mu$ ) and anti-tau ( $\tau^+$ ) with tau anti-neutrino ( $\bar{\nu}_\tau$ ). Quarks also come in three families, with the respective anti-quarks: up ( $u, \bar{u}$ ) and down ( $d, \bar{d}$ ), charm ( $c, \bar{c}$ ) and strange ( $s, \bar{s}$ ), top ( $t, \bar{t}$ ) and bottom ( $b, \bar{b}$ ). The fundamental bosons are the photon ( $A$ ), the W (positively and negatively charged) and Z that mediate the electroweak interaction, the gluon ( $g$ ) mediating the strong interaction and the Higgs ( $H$ ). The weak bosons were discovered at CERN in 1983 at the UA1 and UA2 collaborations over the SPS accelerator (described on section 1.1.1). The Higgs boson has been discovered recently on 2012 by ATLAS and CMS experiments at the LHC. The 2013 physics Nobel prize was awarded to Francois Englert and Peter W. Higgs "for the theoretical discovery of a mechanism that contributes to our understanding of the origin of mass of subatomic particles, and which recently was confirmed through the discovery of the predicted fundamental particle, by the ATLAS and CMS experiments at CERN's Large Hadron Collider".

### 2.2.1 The mass problem

Using the concepts developed on later sections about QFT and symmetries it's possible to construct a whole theory giving rise to a precise description of particles and interactions between them. But such a theory does not allow to have massive bosons, whereas masses for fermions are allowed. A mass term for a fermion  $\psi$  is of the form

$$m_\psi \bar{\psi} \psi$$

where  $m_\psi$  is the mass of the field.

Under  $U(1)$  transformations,  $\psi' = U\psi$ , the mass term remains the same, what means that is invariant under  $U(1)$  transformations. The same is not true for a boson. A mass term for a boson  $A$ , can be written as

$$m_A A^\mu A_\mu \quad (2.9)$$

where  $m_A$  is its mass.

The  $U(1)$  transformation for the boson is  $A'^\mu = A^\mu + \delta^\mu \theta(x)$ . Applying such transformation on the mass term 2.10 one can obtain the transformed term

$$m_A (A^\mu A_\mu + A^\mu \delta_\mu \theta(x) + \delta^\mu \theta(x) A_\mu + \delta^\mu \theta(x) \delta_\mu \theta(x)) \quad (2.10)$$

635 where the last three terms make this term not invariant under  $U(1)$  transformations.  
 636 Consequently, one can say that a mass term for the boson destroy the  
 637 invariance of the theory under  $U(1)$  symmetry.

638 Nonetheless there is no need for a theory of a massive photon, there is a need to  
 639 have massive bosons for weak interactions. There is a relation between the mass of  
 640 a boson and the range of the interaction mediated by it. Massless bosons transmit  
 641 long range interactions, as electromagnetism, but short range interactions, as the  
 642 weak interaction, are mediated by massive bosons. More precisely the interaction  
 643 range is inversely proportional to the mass of the boson, higher the mass shortest  
 644 the range. Such relation can be seen from the structure of the propagator, which  
 645 is a mathematical entity that describes the probability a particle has to travel  
 646 a distance in a given time. Such propagator, for a vector boson, has a generic  
 647 form given in equation 2.11, where  $k_\mu$  is the momentum carried by the boson. It's  
 648 clear from this structure that a massive boson has less probability to travel a long  
 649 distance than a massless boson in a given time.

$$\frac{g_{\mu\nu}}{k^2 - m^2 + i\epsilon} \quad (2.11)$$

650 Then, as massive bosons are requires for weak interaction, somehow the  $SU(2)$   
 651 symmetry has to be broken. There are basically two ways to broke a symmetry:

- 652 • Explicit symmetry breaking: By the introduction of a symmetry breaking  
   653 term in the Lagrangian, as a mass term for the bosons.
- 654 • Spontaneous symmetry breaking: When the ground state of one field fail to  
   655 be invariant under the symmetry.

656 Explicit symmetry breaking is not an option, because the symmetry needs to be  
 657 preserved in the Lagrangian in order to introduce the interaction.

## 658 2.2.2 Spontaneous Symmetry Breaking

659 Several physical systems exhibit an spontaneous symmetry breaking. For example,  
 660 a pencil balanced on its tip is perfectly symmetric system around the vertical axis,  
 661 however, because of the instability of the system the pencil will eventually fall  
 662 over. The final state is stable but not symmetrical. This transition also decreased  
 663 the potential energy of the system, driving the system to its ground state. This  
 664 means that whereas the system had a symmetry the ground state does not show  
 665 the symmetry. In general, symmetry breaking is linked to phase transitions, as  
 666 liquid to gas transition or magnetization of a ferromagnet, covering a plethora of

667 physical processes. To a greater extent, in recent studies, [8], the emergence of life  
 668 has been understood as a phase transition of matter.

669 To achieve an spontaneous symmetry breaking of  $SU(2)$  in QFT one should  
 670 choose a field for which its ground state, vacuum, will fail the symmetry. This  
 671 means, in practical terms, that such field will have a non-zero value in vacuum,  
 672 leading to a presence of particles coming from the field on theory vacua. If a  
 673 fermion field is chosen, the vacuum will show a preference on directionality de-  
 674 pending on its spin orientation, what breaks Poincaré symmetry imposed by spe-  
 675 cial relativity. The same is true if a spin-1 bosonic field is chosen for the task. In  
 676 order to avoid this problem a spin-0 field should be used. In addition, this field  
 677 should be electrically neutral to avoid having a charged vacuum.

678 Whit all this properties in mind, taking a scalar doublet of  $SU(2)$ , defined on  
 679 equation 2.12 where  $\phi^0$  and  $\phi^+$  are complex fields, the most general potential can  
 680 be written from two auto-interaction terms, in equation 2.13.

$$\Phi = \begin{pmatrix} \phi^+ \\ \phi^0 \end{pmatrix} = \begin{pmatrix} \phi^+ \\ \phi_{RE} - i\phi_{IM} \end{pmatrix} \quad (2.12)$$

$$V(\Phi) = \mu^2 \Phi^\dagger \Phi + \lambda (\Phi^\dagger \Phi)^2 \quad (2.13)$$

681 Such potential has a unique minimum for  $\lambda > 0$  and  $\mu^2 > 0$ , but for  $\lambda > 0$  and  
 682  $\mu^2 < 0$  has a set of minima with the shape of “Mexican hat”, shown in figure 2.1.  
 683 Under  $\lambda > 0$ ,  $\mu^2 < 0$  configuration the field breaks spontaneously the symmetry  
 684 reaching the ground state, acquiring an expectation value on vacuum different  
 685 from zero,  $v$ .

### 686 2.2.3 Englert-Brout-Higgs mechanism

687 After the spontaneous symmetry breaking, the scalar doublet transforms into the  
 688 form given in equation 2.14, where  $G^+$  and  $G^0$  are the Goldstone bosons product  
 689 of the breaking of the  $SU(2)$  symmetry, and  $H$  is the Englert-Brout-Higgs boson.  
 690 From Goldstone’s theorem when a symmetry is spontaneously broken a massless  
 691 boson appear for each broken generator. In our specific case, the three generators  
 692 of  $SU(2)$  are broken giving rise to three Goldstone bosons:  $G^+$ ,  $G^-$  and  $G^0$ . This  
 693 massless bosons are “eaten” by the  $W^+$ ,  $W^-$  and  $Z^0$  giving them an additional  
 694 degree of freedom, the longitudinal polarization.

$$\Phi = \begin{pmatrix} G^+ \\ \frac{1}{\sqrt{2}}(H + v - iG^0) \end{pmatrix} \quad (2.14)$$

695 By this mechanism, the  $W$  and  $Z$  bosons acquire mass, being its value set by the  
 696 coupling constant of  $SU(2)$  group and the vacuum expectation value of Englert-

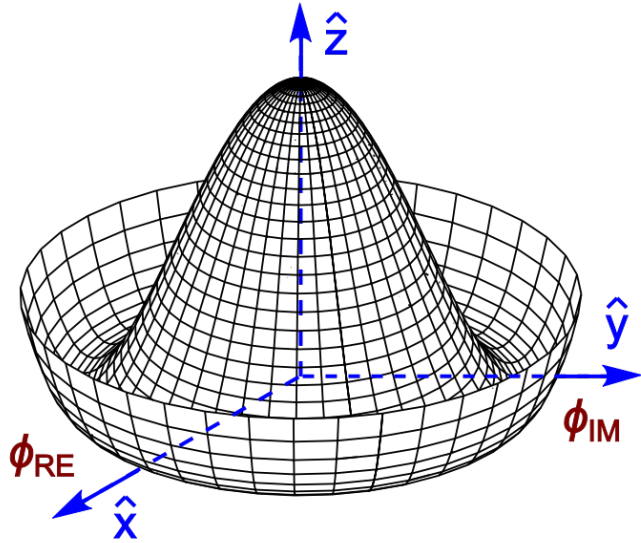


Figure 2.1: Higgs potential

697 Brout-Higgs boson. In addition, the fermions on the theory also acquire a mass  
 698 from the interactions with the scalar doublet. Such masses are in general of the  
 699 form  $m_f = \lambda_f v / \sqrt{2}$ , where  $\lambda_f$  sets the interaction between the Englert-Brout-  
 700 Higgs boson and the fermion. Finally, also the Englert-Brout-Higgs boson has a  
 701 mass  $m_H^2 = -2\mu^2$ .

702 In summary, with this mechanism the weak interaction bosons and fermions of  
 703 the theory are given a mass on the price of introducing an additional scalar field  
 704 to spontaneously break the  $SU(2)$  symmetry.

## 705 2.3 Hierarchy problem and other limitations

706 The SM has been one of the most successful theories on the history of physics.  
 707 With only 19 free parameters, is able to make thousands of predictions that have  
 708 been measured and tested over the last seventy to eighty years. However some  
 709 aspects in the model are not completely understood. The most important one  
 710 is the so-called hierarchy mass problem. At tree level, the Englert-Brout-Higgs  
 711 boson has a mass  $m_H^2 = -2\mu^2$ , but the physical mass also contain the one-loop  
 712 contributions from fermions that interact with it, as the top quark. The Feynman  
 713 diagram for such contribution can be seen in figure 2.2.

714 Such contributions add up giving a mass greater than simple tree level mass.  
 715 Each fermion contributes proportionally to its mass, what means that the top

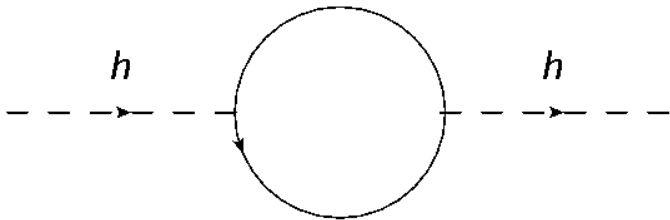


Figure 2.2: One loop diagram for contributions to the mass of the Englert-Brout-Higgs boson from interactions with fermions

716 quark contributes the most. Moreover, if there are in nature heavier fermions that  
 717 also interact with the Englert-Brout-Higgs boson they will also contribute to its  
 718 mass. With such considerations one can expect the Englert-Brout-Higgs boson to  
 719 be much greater than 125 GeV, and in principle not even of the order of 100 GeV  
 720 but greater than 1 TeV. However the real relevance or significance of this problem  
 721 at theoretical level has been discussed extensively, for example at [9], the majority  
 722 of the community agrees there is something to be understood on the subject.

723 The most famous proposed solution to this problem is supersymmetry (SUSY) [10].  
 724 It proposes the existence of an additional symmetry between fermions and bosons,  
 725 at a given point of the history of universe nature didn't distinguish between  
 726 fermions and bosons. However, we know this does not happen at the present,  
 727 and then this symmetry should be broken. Such symmetry implies the existence  
 728 of a super-symmetric partner for each particle, a super-partner. A fermion for each  
 729 boson and vice versa. This SUSY procedure doubles the particle content of the  
 730 model where it's applied. Before breaking SUSY, a particle and it's partner have  
 731 the same mass. In this feature is where the hierarchy problem is solved. On figure  
 732 one can see the one loop diagrams for the mass of the Englert-Brout-Higgs  
 733 boson from the top and its super-partner the stop. Whereas, the top contribution  
 734 is positive, the stop contribution is negative but equal in value, then cancelling  
 735 between them.

736 But this solution works exactly only if SUSY is not broken. As we know SUSY  
 737 has to be broken, there has been developed in the literature different ways to break  
 738 SUSY and still offer a solution to the hierarchy problem, leading normally to solu-  
 739 tions that need a fine adjustment of the parameters of the theory. This represents  
 740 for some theoreticians a problem itself: Fine-tuning or Naturalness. Extensive  
 741 searches for SUSY particles have been performed, accordingly to different model  
 742 realizations MSSM [11, 12], CMSSM, etc.

743 While hierarchy problem is an internal problem of the SM, there are several  
 744 questions that have not been solved. For example, how gravity is understood  
 745 in the frame of QFT's, why there is only 3 generations of leptons and quarks,

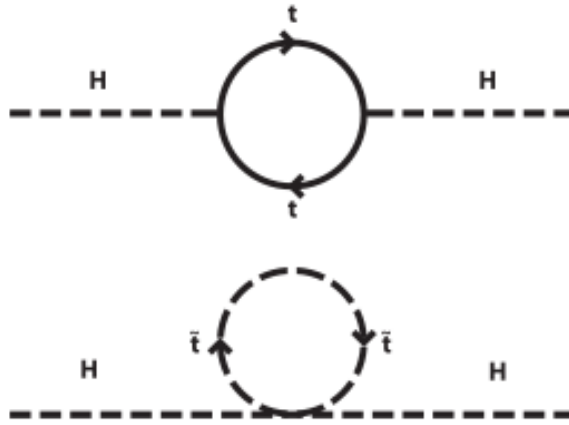


Figure 2.3: One loop diagrams for contributions to the mass of the Englert-Brout-Higgs boson from the top and the stop

746 why there is only 4 fundamental forces among others. In addition, there have  
 747 been experimental questionings to the SM. The mos important one is the masses  
 748 of neutrinos. In the SM neutrinos are massless, careful measurements, [13, 14],  
 749 have shown that neutrinos can oscillate between different flavors, phenomenon  
 750 only possible if neutrinos have a mass. Measurements of solar and atmospheric  
 751 neutrino oscillations have been the most important proof of physics beyond the  
 752 SM.

753 From cosmological measurements, the Wilkinson Microwave Anisotropy Probe  
 754 have shown that the universe is not only made by visible matter, but suggests that  
 755 around 24% its made of dark matter. A type of matter not visible by means of  
 756 light. It has also shown that 71% of the universe is composed of dark energy, what  
 757 makes the universe to be in an accelerated state of expansion. These results can  
 758 be seen in [15, 16]. Also the Planck probe has shown similar results, for example  
 759 in [17]. The SM does not have any answer to this open problems so far.

760 Finally, there is known that the universe presents an asymmetry between mat-  
 761 ter and antimatter, being the first much more abundant than the second. Such  
 762 asymmetry can be obtained by CP-violating processes (C for charge and P for  
 763 parity). However the amount of CP violation present in the SM is not compatible  
 764 with the huge matter-antimatter asymmetry in nature. This problem, known as  
 765 baryon asymmetry, represent an additional huge challenge for particle physics.

766 In conclusion, the SM has been a formidable model that has helped us to under-  
 767 stand a huge amount of physics. It has done thousands of predictions that have

768 been measured and corroborated one by one in the last half-century. However,  
769 this is not the end of the story, perhaps only the beginning. There are theoretical  
770 and experimental motivations that lead us think that the SM is not the “final”  
771 theory that could explain all subatomic phenomena in nature. Currently, there is  
772 a mayor effort, both theoretical and experimentally, to understand and explain all  
773 the remaining pieces. The present work is one of them.

774 In the next chapter, we present an extension of the SM that looks for a solution  
775 to the discussed hierarchy problem.

776 **3 Vector Like Quarks: Generic  
model**

777 778 From chapter 2 we have seen how there are some parts in the SM that does not work very well. From such internal issues some further models/theories have been developed. All this theories are commonly grouped under the term Beyond Standard Model or simply BSM. One of the most famous BSM theory is supersymmetry (SUSY). This theory postulates a symmetry that does not distinguish between fermions and bosons. This idea have given birth to a plethora of model realizations and physics predictions. So far, nothing of the new consequences of this theory have been confirmed but the experiments have an enormous investment on their search. But not only SUSY have seen the day light, there is on the market an astonishing amount of BSM theories addressing different issues of the SM. Extra dimensions, fourth families, composite Higgs are a few of them.

789 In this chapter we will describe a bunch of models that introduce additional heavy quarks, heavier than the top, in order to solve the hierarchy problem, described on section 2.3.

792 **3.1 Motivation**

793 **3.2 Generic Formulation**

794 **3.3 Fesability study for a search of a  $T$  at LHC at 8 TeV**

796 **3.3.1 Production modes**

797 **3.3.2 Decay modes**

798 **3.3.3 Stragey for the full hadronic final state**

799 **3.3.4 Event selection**

800 **3.3.5 Results**

# **801 4 Understanding theory predictions 802 via Monte-Carlo event generation**

803 Although we have nowadays a very elegant and complete theoretical description  
804 of particle physics, is not always evident how to translate this theory in actual  
805 predictions, to compare with measurements. Moreover, on the case of hadronic  
806 colliders, as the LHC, it's even more difficult due to the particularities of strong  
807 interaction. On this subject, a set of tools and approaches have been developed in  
808 order to be able to make accurate predictions from theory that could be directly  
809 researched for on the experiments, as CMS or ATLAS for example. In the present  
810 chapter, we describe such tools and formalisms and a set of studies comparing the  
811 predictions these tools to data.

## **812 4.1 Mote-Carlo simulations**

813 The Monte-Carlo simulations use random numbers and large samplings to calcu-  
814 late mathematical quantities in complex configurations, as integrals or probabili-  
815 ties. The typical example is on how to calculate the integral of a one-dimensional  
816 function. One can throw several random coordinates pair in the Cartesian plane  
817 and count how many of them are under the function. Then the integral of the  
818 function will be proportional to the fraction of points under the curve to the total  
819 thrown points. Larger the number of points, closer the estimation to the real value.  
820 An illustration of the procedure can be seen in figure 4.1.

821 A similar method is used to simulate proton-proton collisions. This simulation is  
822 used to generate “random” events and to calculate quantities, as the cross section,  
823 for a given physical process. Each event represent the final state of a collision, i.e.  
824 the set of particles produced from the collision and seen by a detector. Such simu-  
825 lations comprehend different stages: first, the partonic processes making reference  
826 to the interaction between the partons inside the proton; second, the hadroniza-  
827 tion of the particles produce from parton interactions; and third, the simulation of  
828 the interaction between the hadrons (from second step) and the detector material.  
829 Such events are used to evaluate predictions from theory in the frame of a specific  
830 experiment. Whereas the hadronization and detector simulation are well-known  
831 physical processes, new theories predictions rely basically on the partonic level,

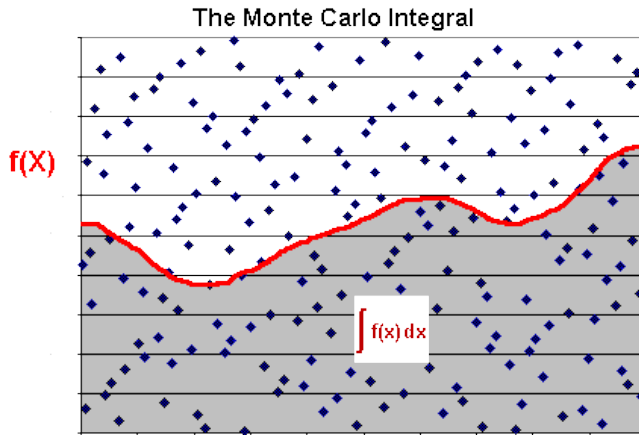


Figure 4.1: Integration using Monte-Carlo methods

832 where the fundamental interaction processes take part.

### 833 4.1.1 Parton simulation

834 The parton model was initially proposed by Richard Feynman in 1969, as a method  
 835 to understand collisions of non-fundamental particles. The model consider a non-  
 836 fundamental particle, as a proton or a neutron, composed of a given number of  
 837 point-like fundamental particles. When a collision occur the point-like particles  
 838 inside have a major probability to scatter. For example, when an electron is fired  
 839 against a proton the most of the interactions will between the electron and the  
 840 fundamental components of the proton,  $u$  and  $d$  quarks. This “hard” components  
 841 are called *valence* quarks. Surrounding them there are the *sea* quarks and gluons.

842 However, as the energy of the collision increases the probability to scatter a sea  
 843 component, quark or gluon, increases. In addition, even if the valence quarks of a  
 844 proton are the  $u$  and  $d$  quarks, heavier quarks can appear in the sea, as the  $b$ ,  $c$  or  $s$   
 845 quarks. The probability to interact with a component, valence or sea, is described  
 846 by parton distribution function, commonly called PDF. A PDF  $f \equiv f(x, Q^2)$  rep-  
 847 resent the number density of a given quark or gluon as a function of the energy  
 848 scale  $Q^2$  and the fraction of momentum carried by the parton  $x$ . The determina-  
 849 tion of a PDF is done via a fit of large data samples from experiments specifically  
 850 designed to test the inner structure of nucleons. The DIS (Deep Inelastic Scat-  
 851 tering) experiment at SLAC (Stanford Linear Accelerator Center), in California,  
 852 United States, first probed the existence of partonic structure inside nucleons us-  
 853 ing leptons as probes scattered against nucleons. Another important experiment  
 854 was the HERA accelerator at DESY in Hamburg, Germany, which used electrons

855 to study the inner structure of protons.

856 In figure 4.2 is shown the Martin-Stirling-Thorne-Watt [18] (MSTW) PDF for  
 857 two energy scales. The MSTW PDF is one of the experimental fits combining data  
 858 from DIS and HERA. In this PDF can be seen that  $u$  and  $d$  quarks carry the most  
 859 of the momentum of the proton. The rest of the momentum is spread mainly over  
 860 a huge amount of gluons and some, less probable, sea quarks as  $\bar{u}, \bar{d}$  or  $c$  and  $s$ .  
 861 One important feature is that the composition of the proton changes depending  
 862 on the energy scale. At  $Q^2 = 10 \text{ GeV}^2$  there is no  $b$ -quark in the proton while at  
 863  $Q^2 = 10^4 \text{ GeV}^2$  there is a non-negligible probability to find it in the proton.

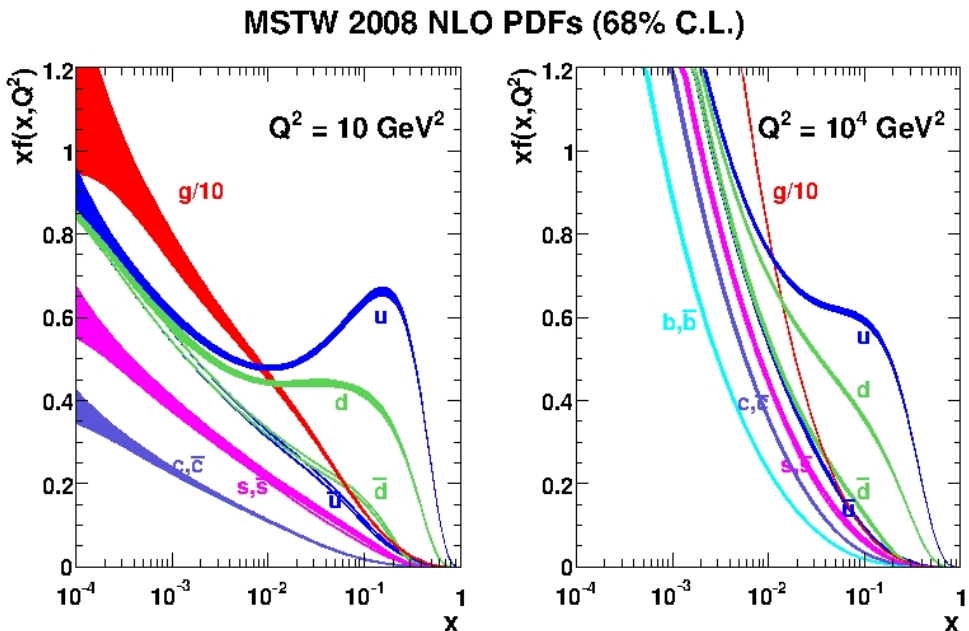


Figure 4.2: Martin-Stirling-Thorne-Watt proton PDF for  $Q^2 = 10 \text{ GeV}^2$  [left] and  $Q^2 = 10^4 \text{ GeV}^2$  [right]. From [18]

864 Two other important PDF fits are CTEQ [19] and NNPDF [20]. Together with  
 865 MSTW, they are the most used PDF sets in the CMS experiment for MC produc-  
 866 tion.

867 For the hard process, the differential cross section can be written as,

$$\begin{aligned}
d\sigma_{ij \rightarrow lm} &= \left( \int_0^1 \int_0^1 f_i(x_i, Q^2) f_j(x_j, Q^2) dx_i dx_j \right) \\
&\times \frac{d^3 p_l}{(2\pi)^2 2E_l} \frac{d^3 p_m}{(2\pi)^2 2E_m} \delta^4(p_i + p_j - p_l - p_m) \\
&\times |\mathcal{M}_{ij \rightarrow lm}|^2
\end{aligned} \tag{4.1}$$

where  $f_{i,j}$  correspond to the PDF's of the initial partons.  $\mathcal{M}_{ij \rightarrow lm}$  is the matrix element of the process which is the part of the S-matrix that contains the amplitude of the process, and modules the transition from the initial to the final state [21]. The matrix element could account effectively for all processes mediating the transition from the initial to the given final state, but in practice it is calculated only including a given number of processes. The calculation can achieve different levels, usually tree level or Leading Order (LO), but modern calculation could arrive, depending on the process, to one loop or Next-to-Leading-Order (NLO) or even two loops the Next-to-Next-to-Leading-Order (NNLO). This limit depends exclusively on the feasibility of the theoretical calculations. In figure 4.3 is shown an example of a leading order plus its corresponding NLO diagrams for a fermion scattering.

### 4.1.2 Hadron simulation

### 4.1.3 Detector simulation

## 4.2 Tools

### 4.2.1 Matrix-element generators

### 4.2.2 Hadron generators

### 4.2.3 Detector simulation

## 4.3 Validation on data

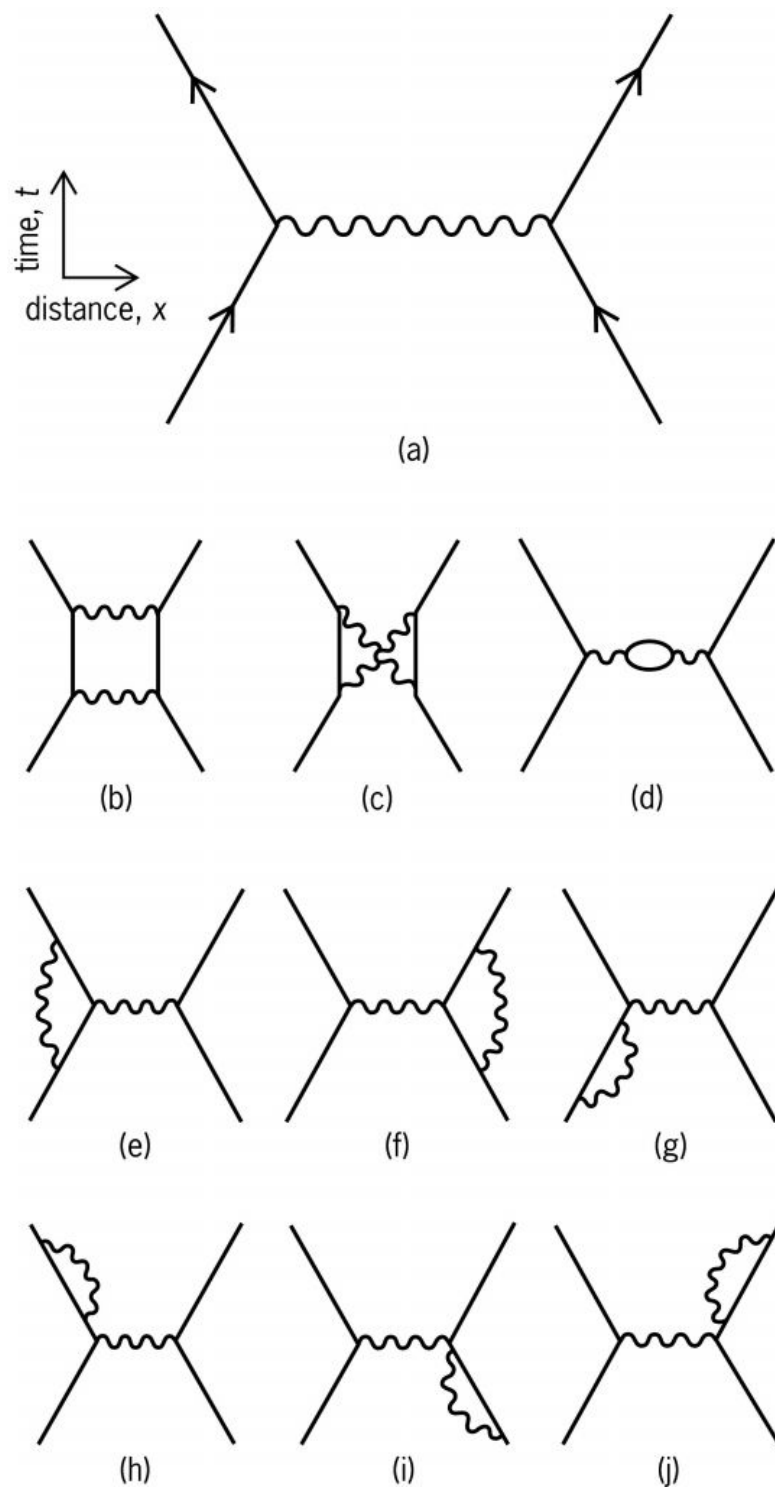


Figure 4.3: LO (a) and NLO (b)-(j) processes contributing to fermions scattering



886 **5 Search for a single produced T'**  
887 **decaying into top and Higgs in**  
888 **the full hadronic final state**

889 In the present chapter we describe in full detail the search performed using 2012  
890 data collected by CMS for a T' in the full hadronic final state. The theoretical  
891 formalism for such object has been described on chapter 3.

892 **5.1 Analysis Strategy**

893 **5.2 Datasets**

894 **5.3 Event selection**

895 **5.3.1 T' reconstruction with a  $\chi^2$  sorting algorithm**

896 **5.3.2 Efficiencies**

897 **Trigger**

898 **Selection**

899 **5.4 Background estimation from data**

900 **5.4.1 Known difficulties and tried methods**

901 **5.4.2 Method**

902 **5.4.3 Validation**

903 **5.5 Systematics**

904 **5.6 Results**

905

# Bibliography

- 906 [1] O. S. Brüning, P. Collier, P. Lebrun, S. Myers, R. Ostoja, J. Poole, and  
907 P. Proudlock, *LHC Design Report*. CERN, Geneva, 2004.
- 908 [2] **CMS Collaboration** Collaboration, G. L. Bayatian *et al.*, *CMS Physics:*  
909 *Technical Design Report Volume 1: Detector Performance and Software*.  
910 Technical Design Report CMS. CERN, Geneva, 2006. There is an error on  
911 cover due to a technical problem for some items.
- 912 [3] **CMS Collaboration** Collaboration, G. L. Bayatian *et al.*, “CMS Physics:  
913 Technical Design Report Volume 2: Physics Performance,” *J. Phys. G* **34**  
914 no. CERN-LHCC-2006-021. CMS-TDR-8-2, (2007) 995–1579. 669 p. revised  
915 version submitted on 2006-09-22 17:44:47.
- 916 [4] **ATLAS Collaboration** Collaboration, A. Collaboration, *ATLAS detector  
917 and physics performance: Technical Design Report*. Technical Design Report  
918 ATLAS. CERN, Geneva, 1999. Electronic version not available.
- 919 [5] **LHCb Collaboration** Collaboration, J. Alves, A. Augusto *et al.*, “The  
920 LHCb Detector at the LHC,” *JINST* **3** (2008) S08005.
- 921 [6] **ALICE Collaboration** Collaboration, P. Cortese, C. W. Fabjan,  
922 L. Riccati, K. Safarík, and H. de Groot, *ALICE physics performance:  
923 Technical Design Report*. Technical Design Report ALICE. CERN, Geneva,  
924 2005. revised version submitted on 2006-05-29 15:15:40.
- 925 [7] **UA4/2 Collaboration** Collaboration, C. Augier *et al.*, “Predictions on the  
926 total cross-section and real part at LHC and SSC,” *Phys.Lett.* **B315** (1993)  
927 503–506.
- 928 [8] C. Mathis, T. Bhattacharya, and S. Imari Walker, “The Emergence of Life  
929 as a First Order Phase Transition,” *ArXiv e-prints* (Mar., 2015) ,  
930 arXiv:1503.02776 [nlin.AO].
- 931 [9] F. Jegerlehner, “The hierarchy problem of the electroweak Standard Model  
932 revisited,” arXiv:1305.6652 [hep-ph].

- 933 [10] S. P. Martin, “A Supersymmetry primer,” *Adv.Ser.Direct.High Energy Phys.*  
 934 **21** (2010) 1–153, [arXiv:hep-ph/9709356 \[hep-ph\]](#).
- 935 [11] **CMS** Collaboration, V. Khachatryan *et al.*, “Search for neutral MSSM  
 936 Higgs bosons decaying to a pair of tau leptons in pp collisions,” *JHEP* **1410**  
 937 (2014) 160, [arXiv:1408.3316 \[hep-ex\]](#).
- 938 [12] **ATLAS** Collaboration, G. Aad *et al.*, “Search for neutral Higgs bosons of  
 939 the minimal supersymmetric standard model in pp collisions at  $\sqrt{s} = 8$  TeV  
 940 with the ATLAS detector,” *JHEP* **1411** (2014) 056, [arXiv:1409.6064 \[hep-ex\]](#).
- 942 [13] **Super-Kamiokande** Collaboration, Y. Ashie *et al.*, “Evidence for an  
 943 oscillatory signature in atmospheric neutrino oscillation,” *Phys.Rev.Lett.* **93**  
 944 (2004) 101801, [arXiv:hep-ex/0404034 \[hep-ex\]](#).
- 945 [14] C. Weinheimer and K. Zuber, “Neutrino Masses,” *Annalen Phys.* **525**  
 946 no. 8-9, (2013) 565–575, [arXiv:1307.3518](#).
- 947 [15] C. L. Bennett, D. Larson, J. L. Weiland, N. Jarosik, G. Hinshaw,  
 948 N. Odegard, K. M. Smith, R. S. Hill, B. Gold, M. Halpern, E. Komatsu,  
 949 M. R. Nolta, L. Page, D. N. Spergel, E. Wollack, J. Dunkley, A. Kogut,  
 950 M. Limon, S. S. Meyer, G. S. Tucker, and E. L. Wright, “Nine-year  
 951 Wilkinson Microwave Anisotropy Probe (WMAP) Observations: Final Maps  
 952 and Results,” *The Astrophysical Journal, Supplement* **208** (Oct., 2013) 20,  
 953 [arXiv:1212.5225 \[astro-ph.CO\]](#).
- 954 [16] G. Hinshaw, D. Larson, E. Komatsu, D. N. Spergel, C. L. Bennett,  
 955 J. Dunkley, M. R. Nolta, M. Halpern, R. S. Hill, N. Odegard, L. Page,  
 956 K. M. Smith, J. L. Weiland, B. Gold, N. Jarosik, A. Kogut, M. Limon, S. S.  
 957 Meyer, G. S. Tucker, E. Wollack, and E. L. Wright, “Nine-year Wilkinson  
 958 Microwave Anisotropy Probe (WMAP) Observations: Cosmological  
 959 Parameter Results,” *The Astrophysical Journal, Supplement* **208** (Oct.,  
 960 2013) 19, [arXiv:1212.5226 \[astro-ph.CO\]](#).
- 961 [17] **Planck** Collaboration, P. Ade *et al.*, “Planck 2015 results. XIII.  
 962 Cosmological parameters,” [arXiv:1502.01589 \[astro-ph.CO\]](#).
- 963 [18] A. Martin, W. Stirling, R. Thorne, and G. Watt, “Parton distributions for  
 964 the LHC,” *Eur.Phys.J.* **C63** (2009) 189–285, [arXiv:0901.0002 \[hep-ph\]](#).
- 965 [19] P. M. Nadolsky, H.-L. Lai, Q.-H. Cao, J. Huston, J. Pumplin, *et al.*,  
 966 “Implications of CTEQ global analysis for collider observables,” *Phys.Rev.*  
 967 **D78** (2008) 013004, [arXiv:0802.0007 \[hep-ph\]](#).

- 968 [20] R. D. Ball, L. Del Debbio, S. Forte, A. Guffanti, J. I. Latorre, *et al.*, “A first  
969 unbiased global NLO determination of parton distributions and their  
970 uncertainties,” *Nucl.Phys.* **B838** (2010) 136–206, [arXiv:1002.4407](https://arxiv.org/abs/1002.4407)  
971 [[hep-ph](#)].
- 972 [21] M. E. Peskin and D. V. Schroeder, *An introduction to quantum field theory*.  
973 Advanced book program. Westview Press Reading (Mass.), Boulder (Colo.),  
974 1995. <http://opac.inria.fr/record=b1131978>. Autre tirage : 1997.



# 975 Contents

976	<b>1 The CMS experiment at LHC</b>	<b>3</b>
977	1.1 The Large Hadron Collider . . . . .	3
978	1.1.1 Injector chain . . . . .	4
979	1.1.2 Main ring . . . . .	6
980	1.1.3 Run 1 . . . . .	9
981	1.1.4 Other experiments at LHC . . . . .	10
982	1.2 The Compact Muon Solenoid (CMS) experiment . . . . .	12
983	1.2.1 Coordinate system . . . . .	15
984	1.2.2 Magnet . . . . .	17
985	1.2.3 Tracker system . . . . .	18
986	1.2.4 Electromagnetic calorimeter . . . . .	19
987	1.2.5 Hadronic Calorimeter . . . . .	20
988	1.2.6 Muon chambers . . . . .	21
989	1.2.7 Trigger . . . . .	23
990	<b>2 The Standard Model</b>	<b>27</b>
991	2.1 Fields, symmetries and interactions . . . . .	28
992	2.2 Quantum fields and particles . . . . .	30
993	2.2.1 The mass problem . . . . .	32
994	2.2.2 Spontaneous Symmetry Breaking . . . . .	33
995	2.2.3 Englert-Brout-Higgs mechanism . . . . .	34
996	2.3 Hierarchy problem and other limitations . . . . .	35
997	<b>3 VLQ models</b>	<b>39</b>
998	3.1 Motivation . . . . .	40
999	3.2 Generic Formulation . . . . .	40
1000	3.3 Fesability study for a search of a $T$ at LHC at 8 TeV . . . . .	40
1001	3.3.1 Production modes . . . . .	40
1002	3.3.2 Decay modes . . . . .	40
1003	3.3.3 Stragey for the full hadronic final state . . . . .	40
1004	3.3.4 Event selection . . . . .	40
1005	3.3.5 Results . . . . .	40

1006	<b>4 MC event generation</b>	<b>41</b>
1007	4.1 Mote-Carlo simulations . . . . .	41
1008	4.1.1 Parton simulation . . . . .	42
1009	4.1.2 Hadron simulation . . . . .	44
1010	4.1.3 Detector simulation . . . . .	44
1011	4.2 Tools . . . . .	44
1012	4.2.1 Matrix-element generators . . . . .	44
1013	4.2.2 Hadron generators . . . . .	44
1014	4.2.3 Detector simulation . . . . .	44
1015	4.3 Validation on data . . . . .	44
1016	<b>5 Single VLQ search</b>	<b>47</b>
1017	5.1 Analysis Strategy . . . . .	48
1018	5.2 Datasets . . . . .	48
1019	5.3 Event selection . . . . .	48
1020	5.3.1 T' reconstruction with a $\chi^2$ sorting algorithm . . . . .	48
1021	5.3.2 Efficiencies . . . . .	48
1022	5.4 Background estimation from data . . . . .	48
1023	5.4.1 Known difficulties and tried methods . . . . .	48
1024	5.4.2 Method . . . . .	48
1025	5.4.3 Validation . . . . .	48
1026	5.5 Systematics . . . . .	48
1027	5.6 Results . . . . .	48